D_____

Award Number: DAMD17-01-1-0677

TITLE: Enabling Technologies for Advanced Soft Tissue Modeling

PRINCIPAL INVESTIGATOR: Steven L. Dawson, M.D.
Mark P. Ottensmeyer, Ph.D.
Robert D. Howe, Ph.D.
Stephane M. Cotin, Ph.D.
Amy Kerdok, Ph.D.
Petr Jordan
Anna M. Galea, Ph.D.
Vincent Luboz, Ph.D.
Maeno Takashi, Ph.D.

CONTRACTING ORGANIZATION: Massachusetts General Hospital
Boston, MA 02114

REPORT DATE: September 2006

TYPE OF REPORT: Final

PREPARED FOR: U.S. Army Medical Research and Materiel Command
Fort Detrick, Maryland 21702-5012

DISTRIBUTION STATEMENT: Approved for Public Release;
Distribution Unlimited

The views, opinions and/or findings contained in this report are those of the author(s) and should not be construed as an official Department of the Army position, policy or decision unless so designated by other documentation.

REPORT DOCUMENTATION PAGE

Form Approved
OMB No. 0704-0188

Public reporting burden for this collection of information is estimated to average 1 hour per response, including the time for reviewing instructions, searching existing data sources, gathering and maintaining the data needed, and completing and reviewing this collection of information. Send comments regarding this burden estimate or any other aspect of this collection of information, including suggestions for reducing this burden to Department of Defense, Washington Headquarters Services, Directorate for Information Operations and Reports (0704-0188), 1215 Jefferson Davis Highway, Suite 1204, Arlington, VA 22202-4302. Respondents should be aware that notwithstanding any other provision of law, no person shall be subject to any penalty for failing to comply with a collection of information if it does not display a currently valid OMB control number. **PLEASE DO NOT RETURN YOUR FORM TO THE ABOVE ADDRESS.**

1. REPORT DATE	2. REPORT TYPE	3. DATES COVERED
01-09-2006	Final	1 Sep 2001 – 31 Aug 2006

4. TITLE AND SUBTITLE

Enabling Technologies for Advanced Soft Tissue Modeling

5a. CONTRACT NUMBER

5b. GRANT NUMBER
DAMD17-01-1-0677

5c. PROGRAM ELEMENT NUMBER

6. AUTHOR(S)
Steven L. Dawson, M.D., Mark P. Ottensmeyer, Ph.D.,
Robert D. Howe, Ph.D., Stephane M. Cotin, Ph.D.,
Amy Kerdok, Ph.D., Petr Jordan, Anna M. Galea, Ph.D.,
Vincent Luboz, Ph.D., Maeno Takashi, Ph.D.

5d. PROJECT NUMBER

5e. TASK NUMBER

5f. WORK UNIT NUMBER

7. PERFORMING ORGANIZATION NAME(S) AND ADDRESS(ES)

Massachusetts General Hospital
Boston, MA 02114

8. PERFORMING ORGANIZATION REPORT NUMBER

9. SPONSORING / MONITORING AGENCY NAME(S) AND ADDRESS(ES)
U.S. Army Medical Research and Materiel Command
Fort Detrick, Maryland 21702-5012

10. SPONSOR/MONITOR'S ACRONYM(S)

11. SPONSOR/MONITOR'S REPORT NUMBER(S)

12. DISTRIBUTION / AVAILABILITY STATEMENT
Approved for Public Release; Distribution Unlimited

13. SUPPLEMENTARY NOTES
Original contains colored plates: ALL DTIC reproductions will be in black and white.

14. ABSTRACT

This report describes a five year research program to develop instrumentation, experimental protocols, mathematical models and tools, and validation techniques to determine and describe the biomechanical behavior of living tissues. The particular focus has been the study of non-load-bearing internal organs that have not been addressed significantly in the literature. These results will contribute to developing realistic simulation tools for medical training and medical device and procedure development. The report summarizes the results of the final year of the project, including completion of a physics-based, tissue model and an algorithm to determine the values of characteristic parameters from experimental data; integration of a 3-D ultrasound scanning system with our indentation instrumentation and algorithms to accurately determine tissue motion; and work to develop new, minimally invasive instruments that would have applications for human use. The report then reviews the work completed over the full course of this program.

15. SUBJECT TERMS
tissue characterization; medical modeling and simulation; surgical training; mathematical modeling

16. SECURITY CLASSIFICATION OF:				18. NUMBER OF PAGES	19a. NAME OF RESPONSIBLE PERSON
					USAMRMC
a. REPORT	b. ABSTRACT	c. THIS PAGE		72	19b. TELEPHONE NUMBER *(include area code)*
U	U	U	UU		

Table of Contents

Introduction **5**

Body **5**

Year 5 Extension Review 5
Ex vivo testing on additional organ systems *6*
Documentation preparation: model description and parameters extracted *7*
Balloon-catheter minimally invasive testing instrument development *8*
Human tissue sourcing and protocol preparation *9*
Real-time implementation of soft tissue models *9*
3-D Optical Flow Field Regularization Using Finite Elements *11*
Improved perfusate recipe and improvements to perfusion system and motorized indentation tester *12*

Full research program summary 14
Instrument and tissue testing protocol development *14*
Modeling, parameter identification and optimization for real-time application *18*
Validation *19*

Key Research Accomplishments **21**

Year 5 Key Research Accomplishments 22

Overall Research Program Accomplishments 22
Instrument and Testing Systems *22*
Modeling and parameter determination *22*
Validation *23*

Reportable Outcomes **23**

Manuscripts 23
Journal Papers *23*
Refereed Conference Papers *23*
Contributed Conference Papers and Abstracts *24*
Related Theses *25*
Lectures, Workshops, Tutorials, Posters *25*
Degrees Completed *26*
Funding applied for based on this work *26*
Employment/Research Opportunities *26*
Databases Established *26*

Collaborations Initiated 27

Personnel supported through this research effort 27

Researchers *27*
Graduate students *27*

Conclusion **27**

References **30**

Appendices **31**

Appendix A Kerdok Thesis - Chapter 4 & Appendix B .....

Appendix B Jordan & Howe Poster .....

Introduction

Fields as diverse as patient safety improvement, body armor solution design, creation of new surgical instruments and rehearsal of new surgical procedures are all benefiting from the creation of computer models of living tissues. These models have applications in surgical simulation systems that allow new doctors to experience their first surgeries without risk to real patients. They can be implemented in finite element models that describe the interaction between an armor solution and the tissue it protects. Doctors and engineers can test new instrument and procedure concepts *in silico*, reducing both the need for animal testing and the time to market or clinical application. This research program has focused on creating mathematical models which capture the behavior of tissues, developing instruments to measure the responses of tissues to controlled loading and deformation, and performing the experiments to determine the characteristic parameters for a variety of non-load-bearing organ tissues *in vivo.* Over the course of the initial four year timeframe, and an additional extension period, we have progressed in all of these areas. Our models have evolved from simple lumped-element tissue models to an advanced seven parameter model which captures the complex non-linear and poro-visco-elastic behavior of organs such as liver, spleen and brain, and we have created mathematical algorithms which enable real-time interactivity with virtual tissues. We have applied pre-existing instruments and developed a series of novel systems to measure the responses of solid organ tissues to small and large deformations and over a wide range of time scales, and we have created an organ perfusion system which enables near-*in vivo* experiments to be performed on the lab bench. Finally, by applying the data acquired in *in vivo* and *in vitro* experiments, we have applied mathematical tools such as inverse finite element analysis to relate the measurements obtained to the models to determine sets of parameters that define the materials tested. This research program has lead to a variety of external collaborations and provides the basis for further research aimed at improving mathematical description and simulation of living tissues.

Body

The following sections present first the results of the work performed during the no-cost extension (NCE) period ("Year 5"), followed by a review of the results achieved and contributions made over the course of the whole research effort. The Year 5 results are presented in the context of the tasks described in the NCE request, similar to the direct comparison with the Statement of Work in the annual reports.

The original proposal objectives and Statement of Work are presented, and the review of the research effort is presented in the context of the three primary areas of work: testing instrument and system development; experimental measurement of tissue responses; and mathematical model development and characteristic material parameter determination.

Year 5 Extension Review

The NCE request was made to make use of funds which remained at the end of the original four year grant period. These funds enabled us to continue to support the researchers and in particular two doctoral candidates for nearly an additional year. The elements of the research program that we proposed were the following:

- Perform ex vivo testing, per the protocols developed for porcine liver, on porcine spleen and kidney, using the extracorporeal perfusion system developed earlier.
- Prepare documentation detailing the model and the parameters extracted from the ex vivo testing.
- Complete development of a balloon-catheter device intended for use ultimately on human tissues, and perform tests with it initially on tissues ex vivo, and if time permits, in vivo on porcine models.
- Establish sources for human tissue samples and prepare protocols for performing tests on these tissues.
- Complete implementation of the mathematical models developed to date into real-time forms suitable for interactive manipulation of virtual organs.

In addition, we continued work on elements from Year 4:

- Developing algorithms to extract 3-D strain field information from 3-D ultrasound scans of tissue, applying 3-D strain data to improving uniqueness of tissue parameter determination.
- Improved perfusate "recipe" (to enable *in vitro* testing to at least 6.5 hours), perfusion system configuration, and motorized indenter hardware
- Maintained and extended external collaborations

Ex vivo testing on additional organ systems

Figure 1 shows a harvested porcine spleen being tested with both the large deformation creep indenter and the motorized indenter system. One goal of this research was to begin to create an atlas of tissue properties across a wide range of tissue types, and the extension of the system to the study of spleen is one of the first steps on this path.

Figure 1: Creep indenter (left rear) and motorized indenter (foreground) testing of porcine spleen.

Typical results from the spleen tests are shown in Figure 2. In Figure 2(a), the indentation strain is recorded over time for a fixed load, exhibiting a similar combination of short

and long term responses observed in our porcine liver tests (see below). Figure 2(b) shows the reaction force of the tissue as the motorized indenter moved at constant speed to an indentation depth of approximately 9mm (roughly equivalent to 30% strain). As can be seen, at higher rates, the reaction forces due to poro-viscous effects are larger than for lower rates. In addition, preliminary results show that the spleen is 10x softer than liver tissue, and seems to be slightly less sensitive to the presence or absence of perfusion, however this result remains to be confirmed over a larger range of experimental conditions.

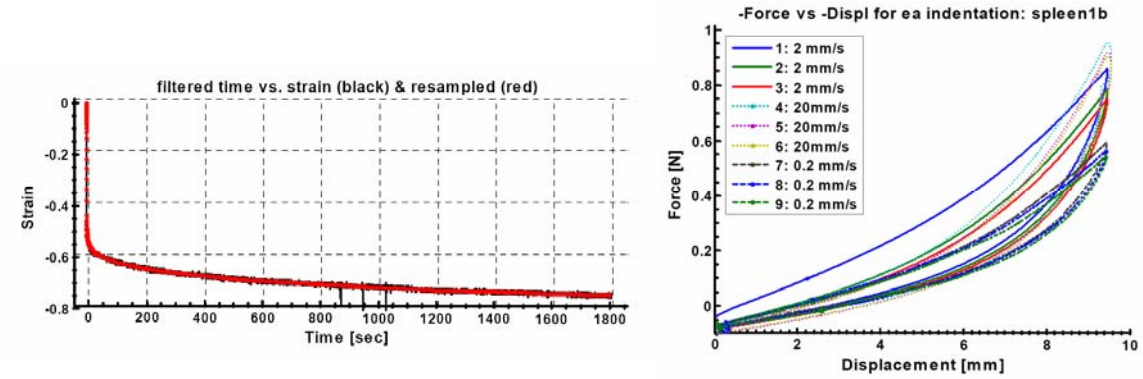

Figure 2: (a) typical creep response of porcine spleen. (b) Series of ramp responses of porcine spleen.

Documentation preparation: model description and parameters extracted

Year 5 saw the completion of the doctoral thesis and successful defense thereof by Dr. Amy E. Kerdok, as well as the printing of our Journal of Biomechanics paper [Kerdok, Ottensmeyer & Howe, 2006]. The pre-print of this paper was included in the 2005 annual report, and Chapter 4 and Appendix B of the thesis are exerpted in Appendix A of this document. Together, these two documents describe the models developed during the course of this research. In brief, Figure 3(A) shows the models used to describe the linear responses from testing using the TeMPeST 1-D device to perform small, sinusoidal deformations over a range of frequencies. This simple model was sufficient to capture the visco-elastic response observed and demonstrate that our perfusion system (described in previous annual reports and in the overall summary below) created conditions much closer to the *in vivo* state than testing tissues in an unsupported *in vitro* state. Figure 3(B) shows the model used to describe the long duration testing performed with our creep-indentation tester, and includes elements to capture both the short time constant behavior and the slower response as fluids within the tissue redistribute over time.

The models of Figure 3 are useful for describing the observed response to the types of indentation performed with our instruments. However, they are not applicable to arbitrary loading modes, and as such, a constitutive model that describes the behavior of liver tissue in general, rather than in these particular experiments, is necessary. The model of Figure 4, described in Appendix A, accounts for constant volume changes in the shape of an element of tissue (e.g. shearing) and changes in its volume as a result of compressibility and porous flow through the tissue. Of the twelve parameters listed in the figure, only seven are independent, and the ranges of values determined from the model optimization process are listed in Table 1. The meaning and derivation of all of the parameters is described in the appendix.

In addition to the full non-linear, poro-visco-elastic model, a simplified linearized version is also described in Appendix A, in the excerpt from Appendix B of Dr. Kerdok's thesis.

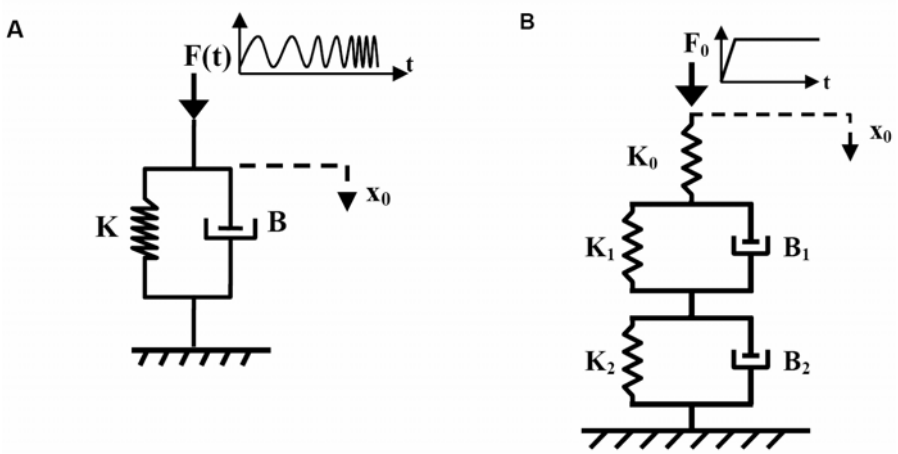

Figure 3: Lumped parameter models of liver tissue. (a) First-order visco-elastic model used to describe TeMPeST 1-D measurement responses. (b) Second-order model capturing short and long time constant behavior of creep response.

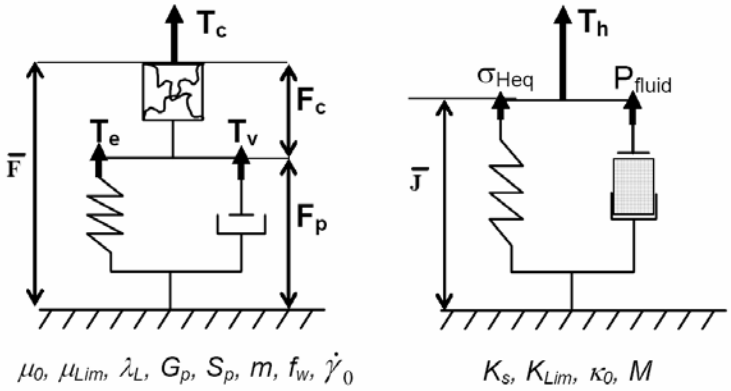

Figure 4: Physically-based, non-linear constitutive soft tissue model. (left) Isochoric (constant volume) response elements. (right) Volumetric response. Model parameters listed for each portion of the model, include both independent and dependent variables.

Table 1: Constitutive model independent parameter ranges

	K_s [Pa]	G_p [Pa]	m	S_p [Pa]	μ_0 [Pa]	λ_L	κ_0 [m^4/Ns]
Parameter range during optimization	6615 - 25 048	40.3 - 116.0	1.18 - 2.50	2393 - 14 214	1.35 - 28.96	1.035 - 1.051	0.86 - 11.2

Balloon-catheter minimally invasive testing instrument development

An ultimate goal of this research has been to move towards making measurements on human tissues *in vivo* as a final validation that the measurements made on human or other tissues *in vitro* with our perfusion system are accurate. With the exception of the TeMPeST 1-D instrument, which was originally designed for minimally invasive surgical use, none of our instruments are suitable for intra-operative use in humans. To address access to human tissues, we observe that the hepatic vein of the liver has an extremely thin layer of epithelium separating the lumen from the parenchyma of the organ. As a result, endovascular measurements of tissue response would allow us to make direct measurements on the parenchymal tissue. Further, since

balloon catheters designed to occlude blood flow through the hepatic vein to measure wedge pressure already exist and are in use, we investigated the possibility of using a balloon catheter to measure the response of parenchyma by inflating a fluid-filled balloon catheter and measuring the pressure-volume response. This measurement is analogous to the force-displacement response made in our indentation testing. Further, by combining these tests with non-invasive 3-D ultrasound scans, we would be able to observe the geometric boundary conditions and the 3-D strain field of the tissue during testing.

While human testing has not been approached to date, we developed the system shown in Figure 5 to examine the feasibility of this technique. As shown in Figure 6, the first balloon expansion shows a response much different from that measured in air. The second and third tests are intermediate between the two, though much closer to the free-air test. We hypothesize that this may be due to tissue damage caused during the first test, but may instead be a normal response of the balloon to initial and repeated tests. We expect to investigate the use of a device of this time further in the future. Given our commitments to completing the documentation and advancing the state of the modeling efforts, *in vivo* tests using the balloon catheter system were not pursued.

Human tissue sourcing and protocol preparation

Despite initial intentions to progress to human tissue testing, none was performed during the course of this research project. In future research programs, we will begin the path towards these tests earlier.

At the present time, we are investigating the procedures necessary to qualify the TeMPeST 1-D instrument for human use, and determine the best methods of sterilizing the instrument. This investigation was commenced in particular as a result of a contract to construct a duplicate of the TeMPeST instrument for Dr. Yohan Payan at Université Joseph Fourier in Grenoble, France. This group seeks to understand the biomechanics of the soft tissues of the human oral cavity, and its effect on the physics of speech production.

Real-time implementation of soft tissue models

A parallel effort under way within the Simulation Group has been the development of an open-source software architecture that will enable researchers from different groups to combine a variety of algorithms for real-time soft tissue deformations, collision detection, graphical and haptic rendering and other elements, into the same simulation system. An international consortium has been formed to develop this framework (called SOFA: Software Open Framework Architecture) lead by Dr. Stephane Cotin, with members at INRIA and TIMC in France, ETH Zurich in Switzerland, the Computer Graphics & Visualization Laboratory in South Korea, and Stanford, Case Western Reserve and UC Berkeley.

One part of this program evolved from the early work on the Truth Cube (TC1) described initially in the Year 1 annual report. The Truth Cube (described in the Validation section, below) was a silicone gel cube with embedded fiducial markers suitable for detection during CT scanning. Large deformations were applied to the TC1, and the motions of the fiducials provided information about the real internal strains, to which mathematical models of deformation can be compared. Research conducted by the SOFA consortium evolved to the point where more complex geometries and real-time modeling techniques have been implemented and are being compared with more complex real object standards such as the cylindrical beam shown in Figure 7.

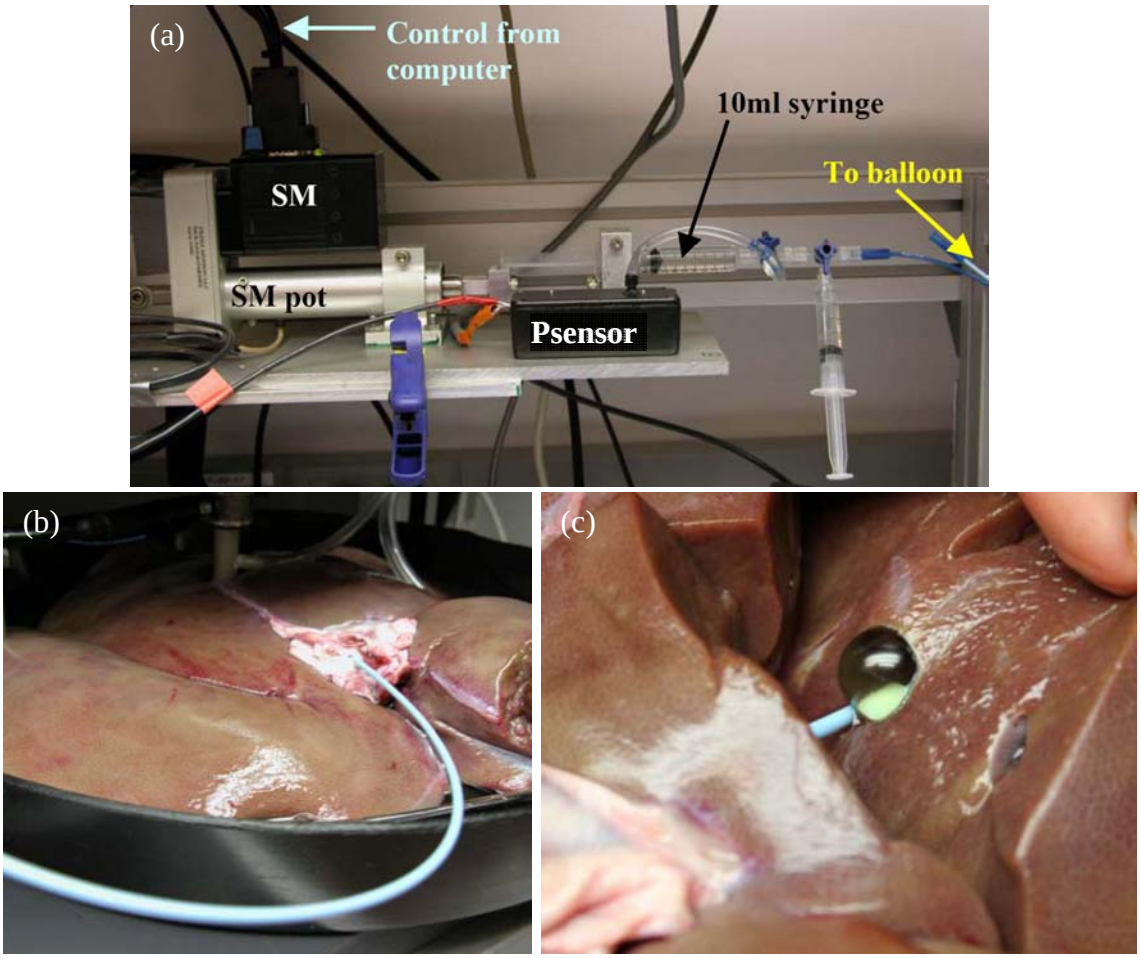

Figure 5: (a) Balloon catheter pressure-volume tester fluid control and sensing apparatus. SM=servomotor; SM pot= servomotor potentiometer; Psensor=pressure sensor. (b) Occlusion balloon catheter inserted into porcine liver hepatic vein. (c) Fluid filled occlusion balloon catheter in hepatic vein in sectioned porcine liver.

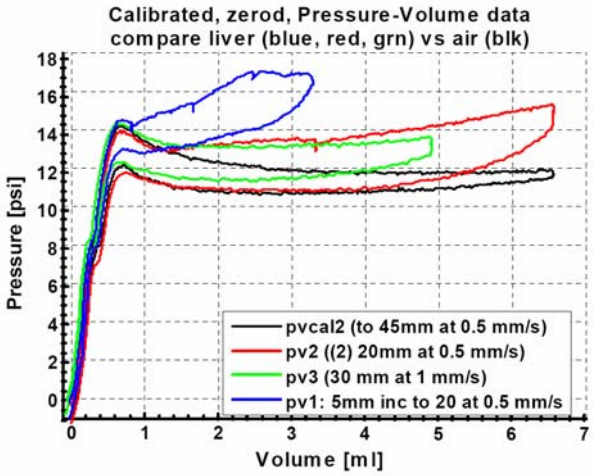

Figure 6: Pressure-volume response of balloon catheter device in air (pvcal2 for calibration) and three tests in porcine liver.

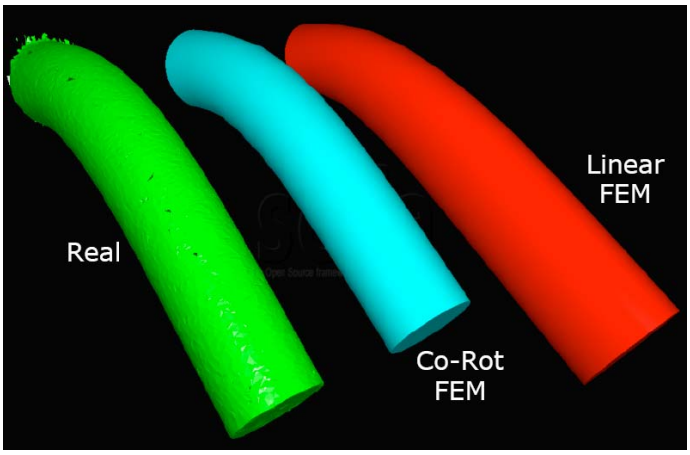

Figure 7: Polymer gel beam reconstructed from CT scan data, and simulated beams using advanced and linear finite element modeling techniques.

The non-linear, poro-visco-elastic model described in Dr. Kerdok's thesis has been provided to SOFA project personnel, who will be investigating integration of a simplified and optimized form into future implementations of SOFA-compatible deformation modules.

3-D Optical Flow Field Regularization Using Finite Elements

During Year 5, we made significant progress in advancing our ability to utilize the data collected from the 3-D ultrasound system that was integrated into our motorized indentation system in Year 4.

In the field of computer vision, a particularly challenging problem is determining the motion of a real scene from a sequence of still images. In general, the problem is insoluble based only on the image data, and require a technique called regularization to add additional constraints beyond the image data to uniquely determine the motions. Mathematical tools exist to perform regularization, but for real deformable objects, a physics-based regularization scheme that makes use of the equations describing elastic and visco-elastic solid-body mechanics has been suggested as a superior technique.

In Year 5, we created such a system for tracking the motion of tissue in three dimensions using the 3-D ultrasound scanner, combining algorithms for estimating local motion with a finite element representation of the same tissue, thereby improving the accuracy of the calculated strain field. This system can then be integrated into the inverse finite element modeling algorithm that we developed previously to improve our estimates of the material parameters that were summarized above from Appendix A.

In essence, a set of virtual springs is attached to each node of a finite element model of the tissue. The ends of the springs are displaced away from the node by an amount related the magnitude of the motion at that location in the optical field. The stiffness of the springs is related to the confidence of the estimate of the local optical flow; where image quality is high, virtual spring stiffness is correspondingly high, and the finite element mesh is tightly bound to the optical (or ultrasound in our case) image. In regions of low image quality, the virtual springs are looser, and the finite element model estimates the true position of a given node given the combination of the tissue constitutive model and the boundary conditions imposed by the other virtual springs.

This algorithm is illustrated in Figure 8, which begins with the estimation of local flow, and ends with a deformed finite element model from which can be calculated the motion of any point within the tissue.

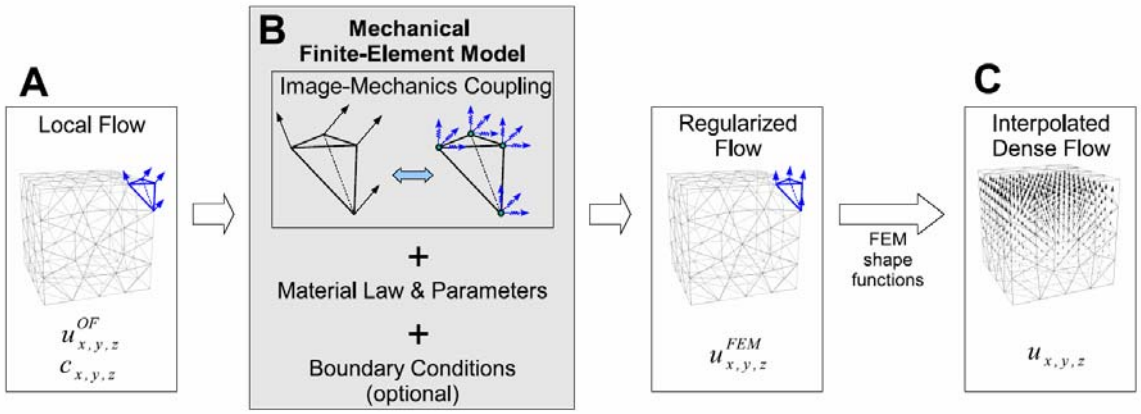

Figure 8: Jordan et al. algorithm for regularizing optical flow calculations through the use of finite element analysis.

Evaluation of this technique has been performed on synthetic data sets created from static ultrasound scans which were deformed using a forward finite element model. The deformed ideal model was degraded with differing levels of Gaussian noise to test how well the algorithm could reconstruct the known deformation from degraded data. An example of the sequence of undeformed ultrasound scan to deformed tissue to reconstructed deformation (uniaxial compression in this case) is shown in Figure 9. Partial details of the technique are described in Appendix B, with full details awaiting acceptance for publication (see Refereed Conference Papers, Jordan et al., 2007)

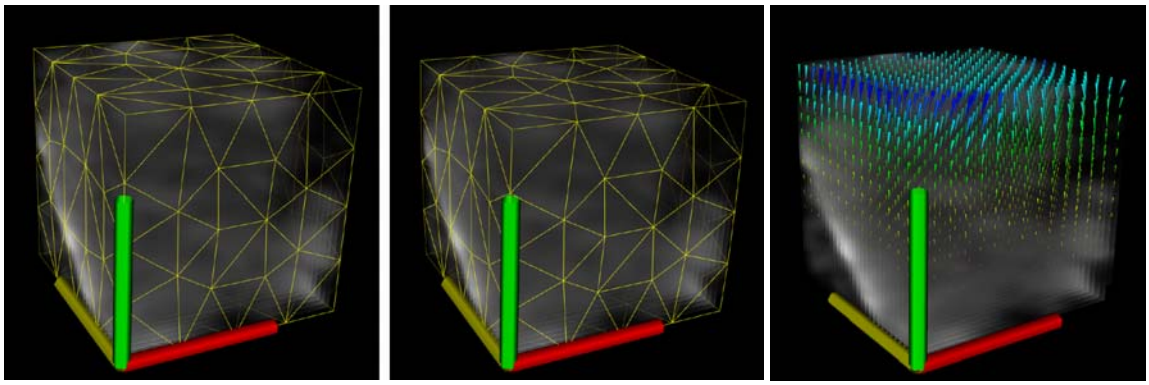

Figure 9: 3-D flow field reconstruction using finite-element regularized optical flow reconstruction algorithm.

Improved perfusate recipe and improvements to perfusion system and motorized indentation tester

As a result of minor observed damage in histological analysis of liver tissue as a result of over-pressure in the perfusion system and the original "recipe" for the perfusate, we continued to improve the perfusion system in Year 5. Specific changes that were made are:

- Install a double-boiler heater to prevent overheating of the perfusate supplied to the arterial reservoir.

- Reduction of the volume of the arterial and venous reservoirs to minimize exposure to room air.
- Alteration of arterial and venous reservoir elevations to reflect porcine blood pressures rather than human blood pressures
- Alteration of the perfusate recipe from heparinized Lactated Ringers Solution to a combination of five liters Dextrose 5% Lactated Ringers Solution to one liter 6% Hetastarch (the heparin used systemically immediately prior to sacrifice and during the initial flush to prevent clotting within the organ)

Histological analysis of tissues maintained under the new perfusion protocol showed less damage even after 6.3 hours of perfusion time (see Figure 10).

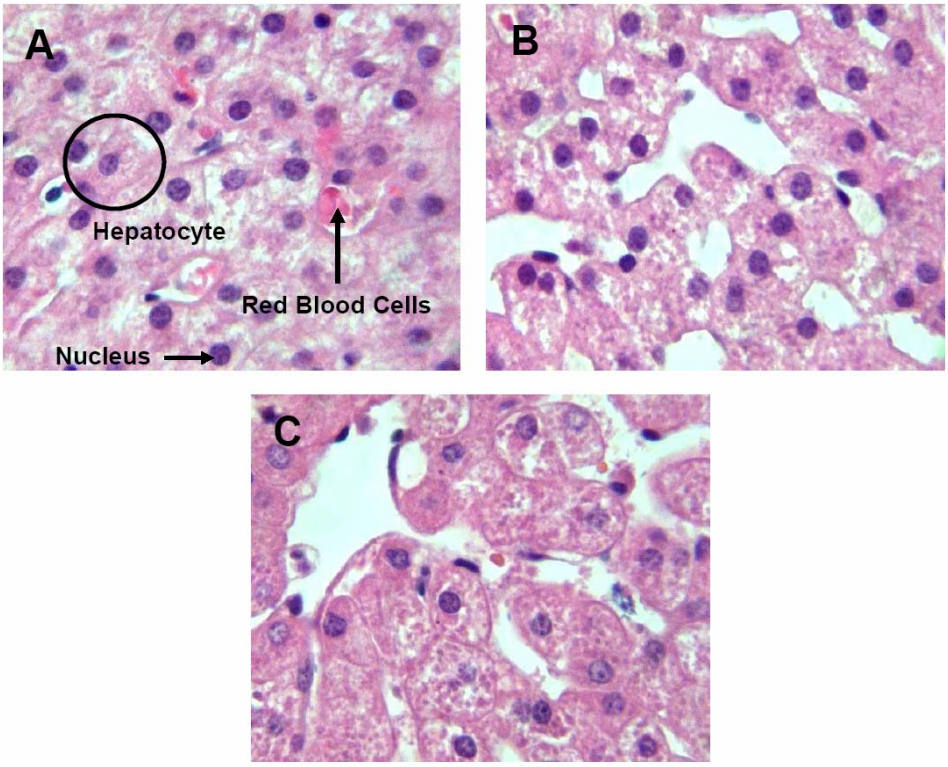

Figure 10: Histological images of porcine liver with H&E staining under 400x magnification. (a) immediately after sacrifice. (b) immediately after initial flush (note lack of red blood cells in vessels) (c) after 6.3 hours of perfusion and 200 minutes of sinusoidal indentation testing. Minimal noticeable difference between (b) and (c).

In addition, the contact head of the motorized indentation tester was replaced with a system that adheres to the tissue sample by application of suction (see Figure 11) through a porous polyethylene filter (to avoid deformation of the tissue). The suction tip improved the non-slip contact between the indenter and the tissue as compared to the original version, which relied on application of a preload force to maintain contact.

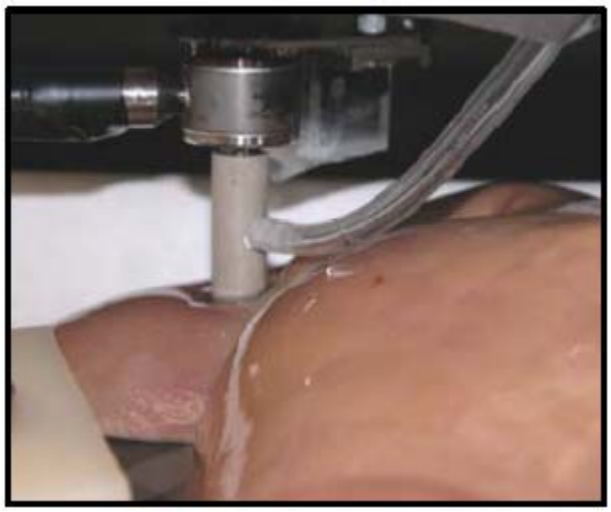

Figure 11: Motorized indenter suction head in contact with porcine liver.

Full research program summary

Our original research proposal laid out a program of essentially three main components working in parallel: create tools and techniques to interrogate the mechanical responses of soft tissues to controlled forces and/or deformations and perform experiments *in vitro* and *in vivo*; develop mathematical models and algorithms to capture the observed tissue responses, determine the values of the characteristic parameters for the tissues in question and generate optimized real-time implementations of the models; and validate our instruments, techniques, and models.

The following sections briefly the progression through the five year effort in each of these areas in turn. Additional details were reported in the earlier annual reports.

Instrument and tissue testing protocol development

At the outset of this work, we had access to the TeMPeST 1-D instrument that was developed by Dr. Mark Ottensmeyer through research previously funded by the Simulation Group. Through a collaboration with Dr. Daniel Kalanovic of the University of Tuebingen, we performed comparisons between indentation and rotary shear by making use of his ROSA2 instrument, demonstrating good agreement on silicone tissue phantoms, but poorer performance during *in vivo* testing, which could not be resolved prior to Dr. Kalanovic's return to Germany (see Figure 12).

Dr. Kerdok and the visiting scientist Dr. Takashi Maeno (Keio University, Japan) developed the T-needle testing system, shown in Figure 13, which examined the response of liver parenchyma deep within the organ by compressing tissue between two cross bars. The complexity of interpreting data from a manually driven version of the instrument lead to motorizing it to improve controllability, however even with this improvement, our mathematical modeling progress was not yet up to the task of determining parameters from the non-uniform stress/strain field between the tips of the T-needles.

Simplifying the geometry of contact with the tissue lead Dr. Kerdok to construct the creep indenter (Figure 14), which also allowed her to measure the long duration response of tissue to a constant load.

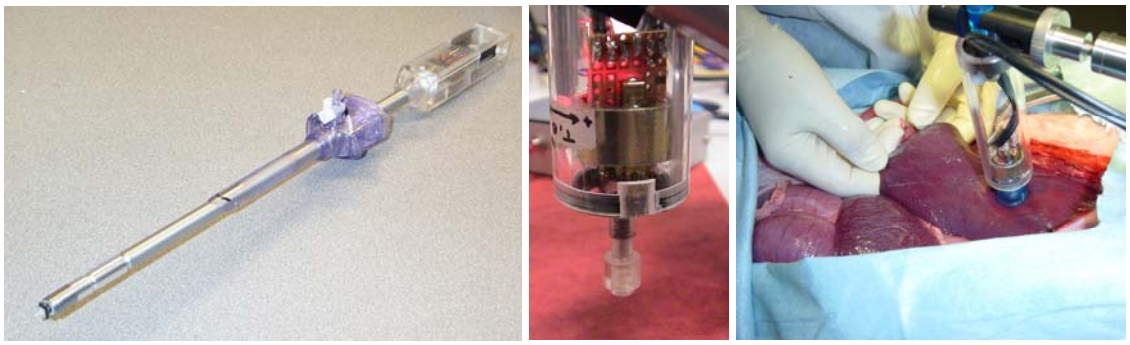

Figure 12: (left) TeMPeST 1-D minimally invasive tissue compliance testing device. (center) ROSA2 torsional shear tester showing rotary shear head (surrounding fixation ring removed). (right) ROSA2 performing *in vivo* measurements on porcine liver.

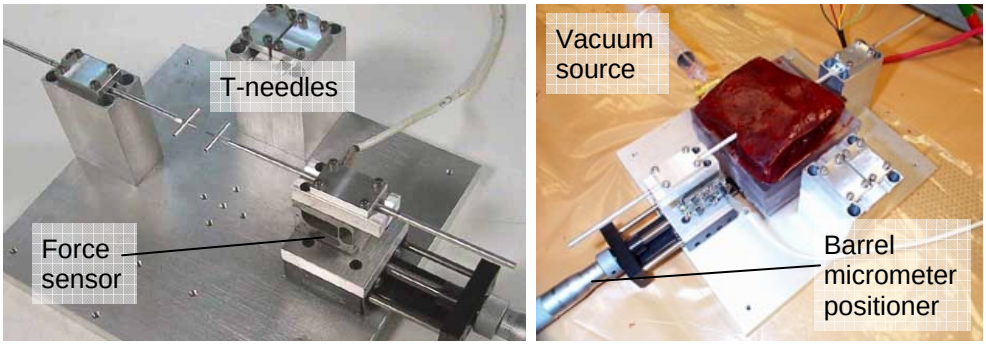

Figure 13: T-needle parenchymal testing instrument. (left) showing T-needles assembled. (right) showing T-needles embedded within porcine liver sample.

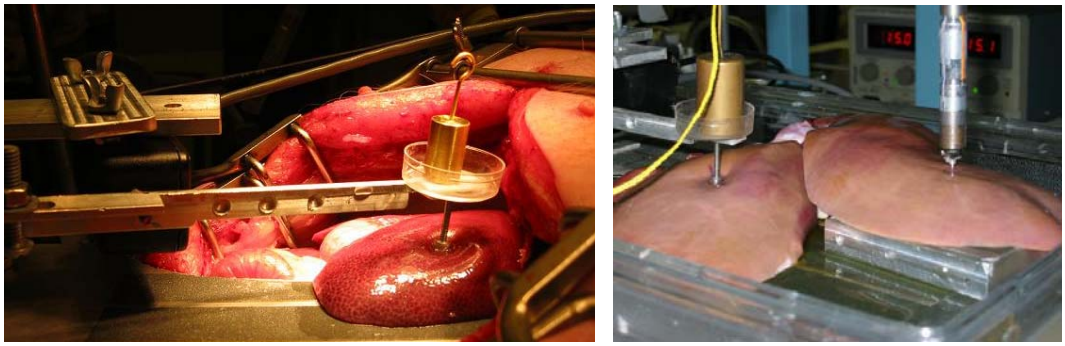

Figure 14: (left) Creep indenter testing porcine liver *in vivo*. (right) Creep indenter and TeMPeST 1-D testing separate lobes of same perfused porcine liver.

As one of the goals was not merely to test the parenchyma of a solid organ, but also its vessels and capsule, Dr. Anna M. Galea applied a tactile probe originally designed to detect lumps within breast tissue (Figure 15), to detecting voids within liver samples. The results of her modeling efforts (described below), showed that the pressure of the fluid within the vessel was more important than the mechanical properties of the vessel walls. In addition, Dr. Kerdok performed tensile testing experiments directly on the liver capsule after carefully harvesting it from the fresh organ and separating it from the underlying parenchymal tissue (see Figure 16).

An early attempt to add imaging technology to our data acquisition armamentarium, and thereby improve our measurements of tissue strain, was the development of a video-based knife-

edge testing system (Figure 15), that could extract the surface contour of a silicone tissue phantom. This technique was superseded by the next series of measurement systems.

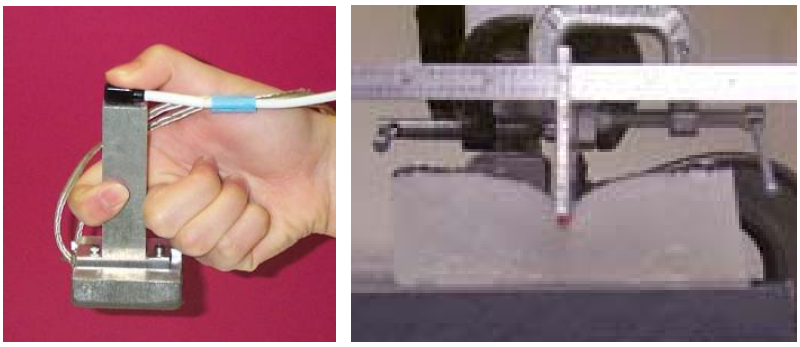

Figure 15: (left) Hand-held tactile probe. Array of force sensor mounted to bottom surface, 3-D position tracking device mounted to top of handle. (right) Video camera view of knife-edge tester (tip highlighted in red) indenting silicone gel tissue phantom.

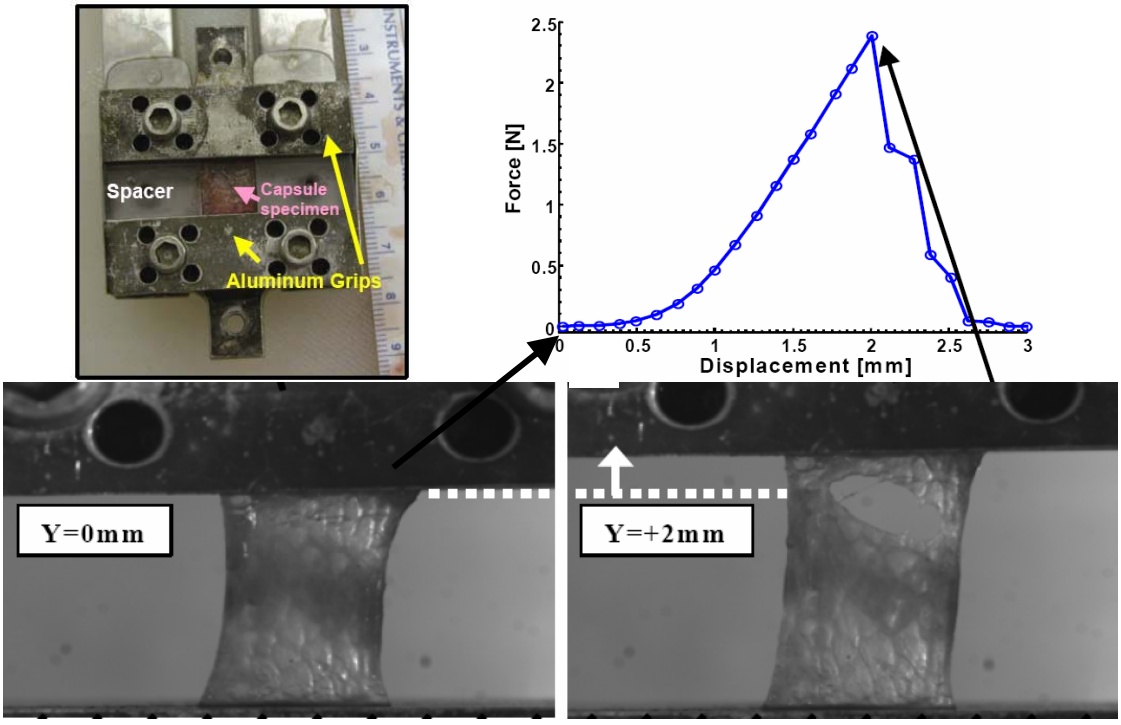

Figure 16: Liver capsule testing system. (top left) Capsule sample holder. (top right) Typical force-displacement response showing non-linear response up to ultimate strength and failure afterwards. (lower left and right) Images of porcine liver capsule undergoing tensile testing.

To greatly improve our ability to apply controlled loads and displacements to tissue, Dr. Kerdok lead the development of the motorized indenter system (based on the TestBench Series high fidelity linear actuator, Bose Corp., EnduraTEC Systems Group, Minnetonka, MN), which can apply larger deformations than the TeMPeST instrument, with a significant fraction of the mechanical bandwidth of that device. She integrated it with the perfusion system that was developed in parallel with the creep indenter, and later, with Petr Jordan, added the scan head of a 3-D ultrasound system beneath the plate on which the tissue samples rest. This last addition enabled us to examine the 3-D strain field within the tissue while the force and displacement of

the indenter tip were simultaneously being recorded, thereby improving our knowledge of the relevant boundary conditions (see Figure 17).

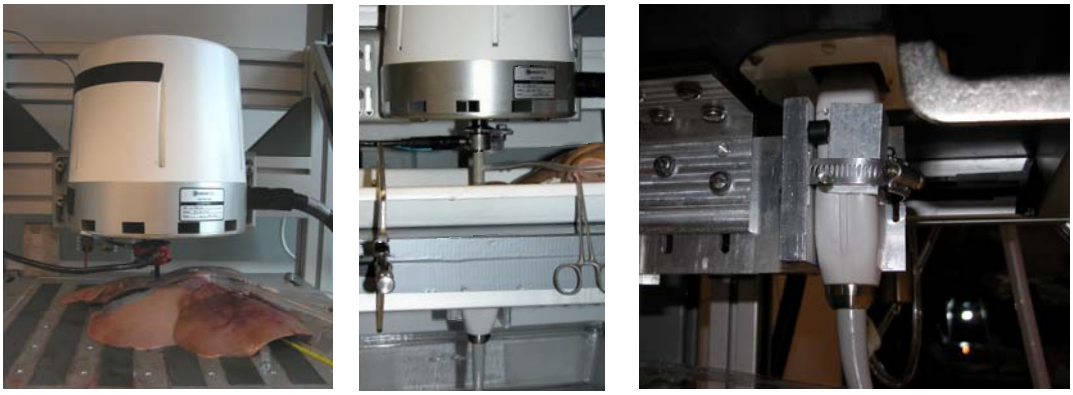

Figure 17: (left) Motorized indentation tester. (center) 3-D ultrasound probe mounted underneath testing platform. (right) Detail of ultrasound probe mounting.

The Normothermic, Extracorporeal Liver Perfusion (NELP) system is a very significant advance over simpler methods of preparing tissues for mechanical testing. By supplying a whole organ with a suitable solution that maintained osmotic pressure and osmolarity, physiological temperature and crucially, physiological blood pressure by elevating reservoirs of physiological solution to provide appropriate hydrostatic pressures, we were able to demonstrate near-*in vivo* test conditions in the *in vitro* environment of the lab bench (Figure 18). The NELP system enabled extended testing (up to 6.3 hours) of tissues, a period significantly longer than would have been possible *in vivo*, and testing in a much more controlled environment that can be achieved intra-operatively.

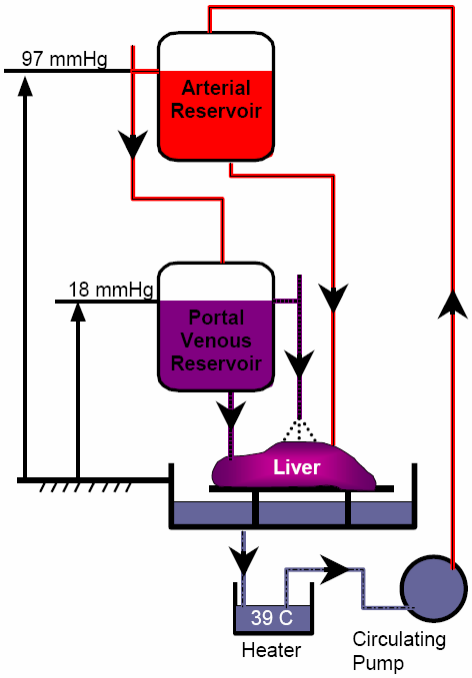

Figure 18: Normo-thermic Extracorporeal Liver Perfusion (NELP) system.

While our research focused mainly on porcine tissues (liver and spleen in particular), through collaborations with other groups, we were able to make *in vitro* and/or *in vivo* measurements on porcine muscle, fat (with Dr. Elisa Konofagou, currently at Columbia University) and brain tissue (with Prof. Simona Socrate, MIT), murine (rat) liver and kidney (with Cynthia Bruyns and Dr. Kevin Montgomery, Stanford University), rat and mouse skin and scar tissue (Dr. Saja Scherer at Brigham and Womens Hospital, Boston), and bovine vocal tissues (Dr. Steven Zeitels, Massachusetts General Hospital, Boston).

Modeling, parameter identification and optimization for real-time application

Our modeling efforts progressed from simple one dimensional first and second order linear approximations of tissue behavior, through application of linear and non-linear finite element modeling techniques to account for tissue testing geometry, to a physics-based constitutive model.

As mentioned above in the summary of Year 5 document preparation, the TeMPeST 1-D measurements were fit to a first order linear model, and the creep indenter data to a second order linear model. The parameters extracted from these models were used to demonstrate the very significant differences in behavior between tissue tested *in vivo* and that tested *in vitro* with no special treatment, and that the use of our perfusion system restored nearly all of the *in vivo* biomechanical characteristics to harvested organs.

The tactile probe described above, had its data analyzed by comparison with finite element models of parenchymal tissue surrounding a pressurized void representing a blood-filled vessel within the tissue (see Figure 19). This modeling effort demonstrated that the tactile probe could be used to identify the presence, size and depth of large vessels.

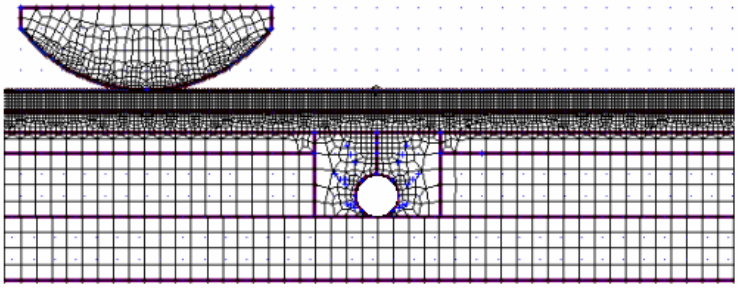

Figure 19: FE model of tactile probe measuring reaction forces of tissue with presurized void. The simulation is repeated with the tactile head moved incrementally across the surface of the simulated tissue.

The most significant advance in our modeling capabilities resulted from a collaboration with Prof. Simona Socrate (MIT), who had previously developed a model for describing the properties of the tissue of the cervix. The model incorporated elements to describe the non-linear character of extra-cellular matrix (collagen, elastin) stiffness, and elements to describe the visco-elastic behavior of the cells and porous flow of fluids through the tissue (see Figure 4, above). Dr. Kerdok adapted the model for use on our liver tissue measurements, and created the inverse finite element modeling techniques that enabled us to identify the parameters of the tissue's constitutive model based on the measurements of surface displacement and applied force. Initial evaluation of the model was done using data collected from force-displacement measurements made on biopsied human breast tumor tissue, collected previously in Dr. Howe's laboratory.

Dr. Kerdok also identified shortcomings of the inverse technique, in that with the limited force-displacement data, it was difficult to uniquely determine the values of the parameters. Mr. Jordan's main contribution was the development of the optical flow techniques described in the Year 5 summary, which convert noisy 3-D ultrasound data into high quality approximations of the true tissue motion within the organ (see Figure 8 and Figure 9). By applying these additional data to the inverse problem, the range of possible characteristic parameters can be significantly narrowed, and this effort will continue on after the research efforts described here.

One of the main applications of the tissue models and parameters determined in this research is the creation of real-time, interactive simulations of surgical interventions for training or pre-operative rehearsal. Dr. Cotin has lead the effort to develop a software architecture, originally known as CAML (common anatomical modeling language) when conceived in late 2000 and early 2001, now in the form of the Software Open Framework Architecture (SOFA). SOFA is a software architecture which can allow the interaction of different real-time representations of tissue deformation, collision, visualization, haptic interaction, and so on. Optimized versions of our non-linear, physics-based, poro-visco-elastic model, will be implemented in the SOFA format for wider distribution and application.

Validation

While our goal is to create accurate models of the deformation of materials that exhibit non-linear stiffness, anisotropy, non-Newtonian porous flow, visco-elasticity and potentially other complex phenomena, we must also verify that our models can accurately describe simple, well characterized materials. To support the model validation effort, and provide a set of gold-standard data to the wider deformable-object modeling community, we created the Truth Cube and its successor standard test objects.

The original Truth Cube was a clear silicone cube (GE RTV6166), 8cm on a side, constructed in layers with Teflon beads embedded in a regular grid with 1cm spacing (see Figure 20). The Cube was subjected to loading conditions including uniaxial compression and hemispherical indentation, while being passed through a CT machine to record not just surface deformations, but also the locations of the displaced Teflon beads. By segmenting the undeformed and deformed scans of the Cube, the internal strain field could be calculated. As a difficult challenge for finite element and other modeling techniques is accurately calculating large deformations, we applied up to 18% uniaxial strain, and 30% nominal hemispherical indentation to the Cube.

The resulting data sets were posted on a dedicated website (http://biorobotics.harvard.edu/truthcube), and compared with finite element simulations, using known material properties of the silicone. In many cases, the mathematical models did not even converge to a solution at the large strain levels.

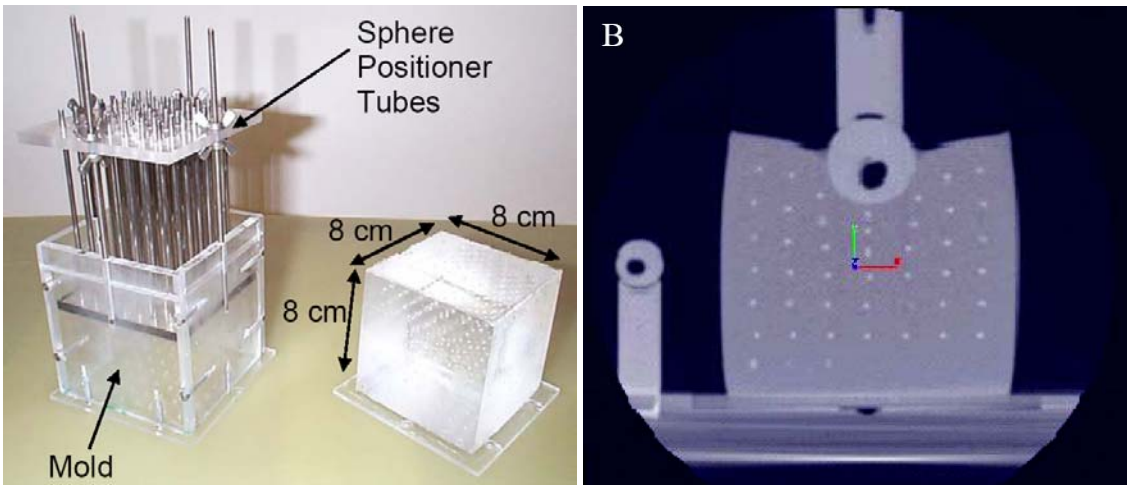

Figure 20: (left) Mold for Truth Cube 1 fabrication and completed Truth Cube 1. (right) CT image through midplane of Truth Cube 1 undergoing spherical indentation.

Subsequent to the Truth Cube testing, we experimented with implanting the Teflon beads into a whole porcine liver and CT scanning the organ in a relaxed state and in a deformed state typical of the organ retraction that would be performed during an operation like a cholycystectomy. This proof-of-concept experiment showed that the use of Teflon fiducial markers was a suitable technique for examining the large strain behavior of whole organs.

Subsequent to the testing of the original Truth Cube, collaborators at ETH Zurich (Switzerland), Nagoya University (Japan) and Brown University encouraged the development of a second standard object that could be shared amongst the groups, tested under their own conditions, and compared against all of the others (the original Cube was destroyed during the final spherical indentation test). Dr. Vincent Luboz (Simulation Group) lead the fabrication of the new (somewhat misnamed…) Truth Cube 2's with Dr. Ottensmeyer (Figure 21). Dr. Marc Hollenstein (then a Ph.D. candidate at ETH Zurich) performed a detailed analysis of the compiled data, providing indications of the scope and applicability of the various testing techniques, and of different methods of simulating the testing methods applied (Hollenstein, 2005).

The SOFA consortium became aware of the Truth Cube series of objects, and recently requested the construction of a new object subject to large deformations. This lead Drs. Luboz and Ottensmeyer to construct cylindrical polymer gel beams which deform under their own weight. Early simulations shown in Figure 22 clearly demonstrate that linear models (which run much faster than more detailed non-linear models) do not predict the deformations of linear materials subject to large strains well, even under static conditions (let alone conditions in which loads and displacements are time varying). This study, supported by separate funding, is ongoing.

Figure 21: Truth Cube 2 (TC2) undergoing torsional resonator testing at ETH Zurich. This test object has randomly distributed Teflon beads embedded within it, rather than the regular grid of beads in TC1. It is made of Ecoflex 0030 (Smooth-On, Inc., Easton, PA)

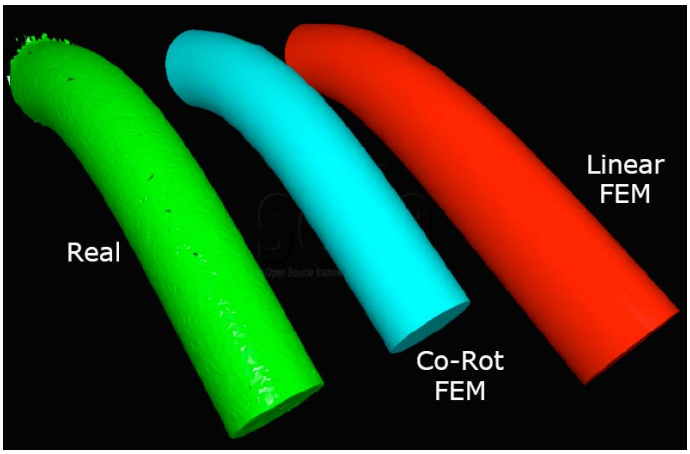

Figure 22: Comparison of Ecoflex 0030 beam under gravity loading (real object segmented from CT scan) with geometrically non-linear and linear FE models.

Key Research Accomplishments

Each of the annual reports listed that year's particular accomplishments. Those of Year 5 are listed here first, followed by an enumeration of the most significant elements of each of the previous years, grouped by category.

Year 5 Key Research Accomplishments

- Extension of tissue testing protocol to porcine spleen, collection of first sets of data. Early estimates show spleen to be 10x softer than liver under similar conditions
- Completion of analysis of liver tissue, including refinement of non-linear, poro-visco-elastic physics-based model and determination of ranges of characteristic parameters
- Initiation of adaptation of model to realtime implementation, with goal of integration within a tissue deformation module compatible with SOFA
- Construction of balloon-catheter-based endovascular tissue testing device. Calibration of balloon elasticity and initial experiments in porcine liver hepatic vein, showing significant differences from balloon inflation in air.
- Development of solid-mechanics-based regularization technique for improving the estimation of 3-D strain field within tissue from 3-D ultrasound scanning data
- Modify the NELP system to correct the hydrostatic pressures of arterial and venous perfusate supplies, improve the controllability of perfusate temperature, add a suction head to ensure non-slip conditions between the indenter head and tissue, and improve the recipe of the perfusate to minimize observable cellular damage during extended perfusion experiments.

Overall Research Program Accomplishments

Instrument and Testing Systems

- Design and construction of T-needle parenchymal tester and motorization of the instrument to enable precise control of motion trajectories
- Evaluation of rotary shear as modality for soft tissue testing
- Design and construction of creep indenter and motorized indenter for large deformation, long duration and high rate testing of whole organ tissues
- Establishment of the Normo-thermic Extracorporeal Liver Perfusion system to enable *in vitro* testing of tissues with ability to capture near *in vivo* mechanical responses
- Integration of 3-D ultrasound scanner with motorized indentation system to better characterize the 3-D strain field generated during indentation

Modeling and parameter determination

- Progression from use of linear, lumped parameter models to describe tissue response to fully 3-D physics-based modeling techniques
- Examination of reaction forces from tactile probe in response to the presence of fluid filled vessels within soft tissues using finite element modeling techniques
- Adaptation of model for rubbery polymers and cervical tissue for application to perfused solid organ tissues
- Creation of inverse finite element optimization technique to determine the seven independent model parameters which characterize a given tissue within the model.
- Establishment of mechanics-based regularization scheme to accurately determine 3-D strain field within deformed tissues
- Conception of common representation and interface specifications for collaborative development of medical simulation algorithms. Initial Common Anatomical Modeling

Language (CAML) concept has "spun-off" into the international Software Open Framework Architecture (SOFA) consortium.

Validation

- Construction and testing of Truth Cube large deformation standard object, comparison of finite element models with measured deformations from CT imagery
- Testing of Teflon fiducial technique as applied to a whole porcine liver
- Collaborative development of Truth Cube 2 standard objects, and comparison of measurement and modeling techniques between groups in the USA, Europe and Japan
- Construction of third generation standard object to examine large deformation of linear material beam configuration to static loading due to gravity. Initial comparison with current state-of-art real-time models

Reportable Outcomes

Manuscripts

Journal Papers

Kerdok AE, Ottensmeyer MP, Howe RD. The Effects of Perfusion on the Viscoelastic Characteristics of Liver, Journal of Biomechanics, 39, 2221-2231, 2006.

Konofagou EE, Ottensmeyer M, Agabian S, Dawson SL, Hynynen K. Estimating localized oscillatory tissue motion for the assessment of the underlying mechanical modulus. Ultrasonics, 42(1-9), 951-6, 2004.

Kerdok AE, Cotin SM, Ottensmeyer MP, Galea AM, Howe RD, Dawson SL. Truth cube: Establishing physical standards for real time soft tissue simulation, Medical Image Analysis, vol. 7, pp. 283-291, 2003.

Ottensmeyer MP. TeMPeST 1-D: an instrument for measuring solid organ soft tissue properties. Experimental Techniques, 26(3), 48-50, May/June 2002.

Refereed Conference Papers

Jordan P, Zickler TE, Socrate S, Howe RD. Mechanical Regularization of Optical Flow: General Framework Using Finite-Elements. Pending submission to IEEE Computer Society Conference on Computer Vision and Pattern Recognition, Minneapolis, MN, 18-23 June 2007.

Liu Y, Kerdok AE, Howe RD. A nonlinear finite element model of soft tissue indentation, in S. Cotin and D.N. Metaxas, eds., Proceedings of Medical Simulation: International Symposium - ISMS 2004, Cambridge, MA, June 17-18, 2004, Lecture Notes in Computer Science vol. 3078, Springer-Verlag, pp.67-76.

Ottensmeyer MP, Kerdok AE, Howe RD, Dawson SL. The effects of testing environment on the viscoelastic properties of soft tissues, , in S. Cotin and D.N. Metaxas, eds., Proceedings of Medical Simulation: International Symposium - ISMS 2004, Cambridge, MA, June 17-18, 2004, Lecture Notes in Computer Science vol. 3078, Springer-Verlag, pp.9-18.

Galea AM, Howe RD. Liver Vessel Parameter Estimation from Tactile Imaging Information, in S. Cotin and D.N. Metaxas, eds., Proceedings of Medical Simulation: International Symposium - ISMS 2004, Cambridge, MA, June 17-18, 2004, Lecture Notes in Computer Science vol. 3078, Springer-Verlag, pp. 59-66.

Bruyns C, Ottensmeyer M. Measurements of Soft-Tissue Mechanical Properties to Support Development of a Physically Based Virtual Animal Model. Dohi T and Kikinis R, eds. Proceedings of MICCAI 2002, Laboratory Notes in Computer Science 2488, 35-43, Springer-Verlag, Berlin. 25-28 Sept. 2002, pp282-9.

Kerdok AE, Cotin SM, Ottensmeyer MP, Galea AM, Howe RD, Dawson SL. Truth cube: Establishing physical standards for real time soft tissue simulation International Workshop on Deformable Modeling and Soft Tissue Simulation, Bonn, Germany, 2001.

Contributed Conference Papers and Abstracts

Valtorta D, Hollenstein M, Nava A, Luboz V, Lu M, Choi A, Mazza E, Zheng YP, Cotin SM. Mechanical characterization of soft tissues: comparison of different experimental techniques on synthetic materials Proceedings of the 4th International Conference on the Ultrasonic Measurement and Imaging of Tissue Elasticity, Lake Travis, Austin, Texas, USA, October 2005.

Jordan P, Kerdok AE, Socrate S, Howe RD. Breast Tissue Parameter Identification for a Nonlinear Constitutive Model in Proceedings of the BMES conference in Baltimore, MD, 2005.

Kerdok AE, Howe RD. Characterizing Large Deformation Behavior of Liver for Surgical Simulation, in Proceedings of BMES, Baltimore, MD, 2005.

Kerdok AE, Howe RD. A Physical Basis for a two Time Constant Constitutive Model for Liver, submitted to the 2005 ASME Summer Bioengineering Conference, June 22-26, Vail Cascade Resort & Spa, Vail, Colorado, 2005. **(honorable mention, PhD student poster competition)**

Kerdok AE, Jordan P, Liu Y, Wellman P, Socrate S, Howe RD. Identification of Nonlinear Constitutive Law Parameters of Breast Tissue, submitted to the 2005 ASME Summer Bioengineering Conference, June 22-26, Vail Cascade Resort & Spa, Vail, Colorado, 2005.

Kerdok AE, Socrate S, Howe RD. Soft tissue modeling and mechanics, 28th American Society of Biomechanics Annual Conference. X-CD Technologies Inc., Portland, OR. poster 235, 2004.

Kerdok AE, Howe RD. A Technique for Measuring Mechanical Properties of Perfused Solid Organs, ASME Summer Bioengineering Conference, Key Biscayne, FL, 2003.

Kalanovic D, Ottensmeyer MP, Gross J, Buess G, Dawson SL. Independent testing of soft tissue visco-elasticity using indentation and rotary shear deformations. Proceedings of Medicine Meets Virtual Reality 11, Newport Beach, CA. IOS Press. pp137-143. Jan 22-25 2003.

Ottensmeyer MP. In vivo measurement of solid organ mechanical tissue properties. Society for Experimental Mechanics Annual Meeting, Milwaukee, WI. pp328-333. 10-12 June 2002.

Ottensmeyer MP. In vivo measurement of solid organ visco-elastic properties. MMVR02/10. Proceedings of Medicine Meets Virtual Reality 02/10, Newport Beach, CA. IOS Press. pp328-33. 23-26 Jan 2002.

Kerdok AE. Soft Tissue Characterization: Mechanical Property Determination from Biopsies to Whole Organs, Whitaker Foundation Biomedical Research Conference. August 9-12, 2001, La Jolla, CA. (Poster)

Cotin S, Dawson S. CAML: a general framework for the development of medical simulation systems. Proceedings of SPIE; 2000. p. 294-300.

Cotin S, Shaffer D, Meglan D, Ottensmeyer M, Berry P, and Dawson S, CAML: a general framework for the development of medical simulation systems. Proceedings of the SPIE

conference on Digitization of the Battlespace and Battlefield Biomedical Technologies, Orlando, 2000.

Related Theses

Amy Elizabeth Kerdok. Characterizing the Nonlinear Mechanical Response of Liver to Surgical Manipulation, Doctoral Thesis, Department of Engineering and Applied Sciences, Harvard University, Cambridge, MA, 2006

Marc Hollenstein. Mechanical Characterization of Soft Materials, Diploma (doctoral) Thesis, ETH Zurich, 2005.

Lectures, Workshops, Tutorials, Posters

Dawson SL, Ottensmeyer MP, Kerdok AE, Howe RD. Enabling Technologies for Advanced Soft Tissue Modeling, presented at PRMRP Military Health Research Forum, San Juan, PR, 30 April – 4 May 2006. Poster and oral presentations.

Ottensmeyer MP, Neumann PF. Physical and Virtual Simulators for Medical Training, Dartmouth College, Engineering Science 05: Healthcare and Biotechnology in the 21st Century, 23 May 2006

Kerdok AE, Howe RD, Dawson SL, Socrate S. Mechanical characterization of liver for surgical simulation. Presented at Industrial Outreach Program. Harvard University, 2005. (poster presentation)

Kerdok AE, Howe RD. Characterizing Large Deformation Behavior of Liver for Surgical Simulation, HST Forum, Boston, MA. (poster presentation)

Jordan P, Howe RD. Identifying the Parameters of a Nonlinear Constitutive Law for Soft Tissue Using Three-Dimensional Ultrasound Imaging. HST Forum, Boston, MA. (poster presentation)

Ottensmeyer, MP. Biomedical Engineering (and stuff…), Shad Valley Dalhousie, summer science program for high school seniors. 26 July 2004

Dawson SL, Ottensmeyer MP, Kerdok AE, Howe RD. Enabling Technologies for Advanced Soft Tissue Modeling, presented at PRMRP Military Health Research Forum, San Juan, PR, 25-28 April 2004. Poster and oral presentations

Kerdok AE. The Effects of Testing Environment on Soft Tissue Properties, presented at HST Forum, Boston, MA, 2004.

Ottensmeyer MP. Tools for measuring soft tissue properties. Workshop on Reality-Based Modeling of Tissues for Simulation and Robot-Assisted Surgery, at IEEE/RSJ IROS 2003, 31 Oct 2003

Ottensmeyer MP. Measuring properties of living tissue or How to make Virtual Organs feel right. Dartmouth College, Engineering 013: Biotechnology and Virtual Medicine, 29 July 2003

Ottensmeyer MP. In vivo measurement of the mechanical properties of soft tissues. McMaster University, Mechanical Engineering Seminar Series, 16 June 2003

Ottensmeyer MP. In vivo measurement of the mechanical properties of soft tissues. City College of New York, City University of New York, Dept. of Biomedical Engineering Seminar Series, 15 Apr 2003

Kerdok AE, Howe RD. Measuring Parenchymal Properties of Perfused Solid Organs, MIT Health Sciences and Technology 2003 Forum Abstract

Ottensmeyer MP, Kalanovic D, Gross J. Comparison of indentation and rotary shear as modes for interrogating soft tissue visco-elasticity, SMIT2002, Annual Conference of the Society for Medical Innovation and Technology, Oslo, Norway, 5-7 Sept 2002.

Ottensmeyer MP. In vivo measurement techniques for determining mechanical responses of soft tissues. Tufts University Mechanical Engineering Seminar Series, 10 Apr 2002.

Ottensmeyer MP. In vivo measurement of solid organ stiffness. Stanford Workshop on Surgical Simulation, Stanford University, Stanford, CA, 20-22 June 2001.

Ottensmeyer MP. Design of Devices for Tissue Property Measurement and Haptic Display. Part of half-day tutorial on medical simulation and training: "Simulating minimally invasive surgical procedures in virtual environments: From tissue mechanics to simulation and training" Medicine Meets Virtual Reality 2000, Newport Beach, CA, 27-30 Jan 2000.

Degrees Completed

Ph.D. Thesis
Kerdok, A.E.

Funding applied for based on this work

- Medical Simulation Trainin Initiative. PI: Dawson SL. Sponsor: RAD II/CCC. 10/1/2006-9/30/2011 (proposal in preparation)
- Collaborative Development of an Open Framework for Medical Simulation. PI: Cotin SM. Sponsor: Telemedicine and Advanced Technology Research Center, US Army. 1/1/2006-12/31/2006
- Evaluation of Wound Healing and Scar Formation Using Mechanical Impedance Test. PI: Ottensmeyer MP. Sponsor: CIMIT, under Department of the Army, cooperative agreement no. DAMD17-02-2-0006. Proposal rejected.
- Construction of Duplicate TeMPeST 1-D for Dr. Yohan Payan, TIMC. PI: Ottensmeyer MP. Sponsors: Université Joseph Fourier & Project MIDAS, Grenoble, France. 12/1/2005-2/1/2006
- Simulation of Behind-armor Effects of Ballistic Threats. PI: Ottensmeyer MP. Sponsor: CIMIT, under Department of the Army, cooperative agreement no. DAMD17-02-2-0006. 1/1/2004 – 12/12/2004
- Development of Vocal Tissue Property Measurement Instrumentation. PI: Ottensmeyer MP. Sponsor: Massachusetts Eye and Ear Infirmary. 11/15/2003 – 11/15/2004

Employment/Research Opportunities

Dr. Amy E. Kerdok is now performing post-doctoral research with Prof. Simona Socrate, Dept. of Mechanical Engineering, MIT. This is an extension of the physics-based modeling research elements of this program.

Databases Established

Results of the original Truth Cube standard object CT scans have been archived and made publicly available at:

http://biorobotics.harvard.edu/truthcube

Collaborations Initiated

- SOFA: Simulation Open Framework Architecture (ongoing)
  USA: Simulation Group, MGH; Stanford Bio-computation Lab, Stanford; Case Western Reserve University, UC Berkeley. Europe: INRIA (Alcove, Evasion, Epidaure Groups); TIMC, ETH Zurich. Asia: Computer Graphics & Visualization Lab (South Korea)
- Simulation of Behind-armor Effects of Ballistic Threats (ongoing)
  Simulation Group, MGH; Institute for Soldier Nanotechnologies, MIT
- Truth Cube 2 (ongoing)
  USA: Simulation Group, MGH; Brown University. Europe: ETH Zurich. Asia: Nagoya University.
- Validation of Harmonic Motion Imaging of Soft Tissue Lesions with Indentation Testing (5/2003-2/2004)
  Simulation Group, MGH; Dept of Radiology, Brigham and Women's Hospital.
- Comparison of Rotary Shear with Normal Indentation Soft Tissue Measurements (4/2002-10/2002)
  USA: Simulation Group, MGH; Germany: Section for Minimally Invasive Surgery, University of Tuebingen.
- Microgravity Rat Dissection Simulator (12/2001-8/2002)
  Simulation Group, MGH; National Biocomputation Center, Stanford University; Center for Bioinformatics, NASA Ames.

Personnel supported through this research effort

Researchers

Massachusetts General Hospital:
Dr. Steven L. Dawson, M.D., (PI) Department of Radiology, The Simulation Group,
Dr. Stephane M. Cotin, Ph.D., The Simulation Group
Dr. Mark P. Ottensmeyer, Ph.D., The Simulation Group
Dr. Xunlei Wu, Ph.D., The Simulation Group

Harvard University
Dr. Robert D. Howe, Ph.D., (Co-I) Department of Engineering and Applied Sciences
Dr. Takashi Maeno, Ph.D., visiting scientist, currently in Department of Mechanical Engineering, Keio University, Japan

Graduate students

Department of Engineering and Applied Sciences, Harvard University
Dr. Amy E. Kerdok, Ph.D.
Dr. Anna M. Galea, Ph.D.
Petr Jordan, S.M.

Conclusion

When this research program was proposed in 2001, the field of measurement and modeling of soft tissues *in vivo* was considered to be a "black hole"; while cadaver and animal tissues have been measured *in vitro* for decades, there was a significant absence of data available

for those wishing to create simulations of the deformation of living tissues. As discussed in the Introduction, a variety of applications require better mathematical descriptions of tissues, including surgical simulation for training, procedure planning and instrument design (revolving around improving patient safety) and others such as high rate impact simulation for the design of body armor solutions (with the expectation of reducing the incidence of trauma).

This program specifically addressed the parallel problems of: creating instrumentation and protocols to perform controlled loading and deformation experiments on tissues *in vivo* and (properly prepared) tissues *in vitro*; developing mathematical models to interpret the data collected; and validating the simplified, optimized models created to do real-time approximations of the fully detailed versions.

We examined the types of *in vivo* testing devices that had been described in the literature at the outset of the program, and determined that none met the needs that we expected in terms of providing repeatability, well defined geometry and range of tissue strains and strain rates achievable. As a result, we initiated a program to create novel instruments to address these issues, progressing from the existing TeMPeST 1-D instrument to the motorized indenter combined with a 3-D ultrasound scanner. A major contribution of the measurement part of the research was the establishment of the perfusion system to enable extended testing of whole organs in a near *in vivo* state. The perfusion system provides a more well controlled environment than the abdominal cavity of a test animal in the operating room, and enables the use of organs harvested from other researchers' approved non-survival experiments. This latter capability reduces the need to sacrifice additional animals only for the purpose of harvesting one organ.

As our instrumentation advanced, our mathematical modeling tools evolved as well. Simple linear, first and second-order models sufficed to demonstrate that the perfusion system created the desired environment, and that unperfused tissues behaved very differently from tissues *in vivo*. These models are not constitutive models suitable for simulating the generic deformations that would be generated in a useful surgical simulator, and as a result we adopted and implemented a modified version of a physics-based, non-linear, poro-visco-elastic model which captures many of the observed behaviors of tissues. To determine the values of the independent parameters that characterize a given organ, we implemented the model as part of an inverse finite element optimization algorithm. This algorithm begins with trial values of the parameters, calculates the simulated response given known boundary conditions, and produces an output which is compared to measurements made experimentally. The parameter estimates are updated based on the difference between real and simulated data until the two are in close agreement. The use of this algorithm has allowed us to determine a range of possible values for the seven parameters that correspond with the observed real responses.

To improve the utility of the model, we wish to reduce the calculated range of the parameters, which results from force and displacement data that is insufficient to yield a unique determination. This uniqueness problem has been addressed through the development of the optical flow techniques described above, which are now ready to be implemented within the inverse FE algorithm to narrow the range of the characteristic parameters.

As models cannot be assumed to be accurate by comparing them with simulations of themselves, we established the series of standard test objects that have come to be known as Truth Cubes. These polymer gel objects with internal fiducials have been scanned under a variety of loading conditions, and serve as a gold standard against which current and future soft tissue deformation models can be evaluated.

This body of work has resulted in:

- publication of nine peer-reviewed scientific journal and conference papers
- publication of thirteen contributed scientific conference papers
- two doctoral theses, one on the soft tissue modeling and measurement, the other on the Truth Cube series of objects and an international collaboration to compare different measurement and modeling techniques
- at least 17 seminars, poster presentations, workshop lectures and other research communications
- six grant proposals or contracts stemming from the expertise established in instrument development, soft tissue characterization and mathematical modeling
- six national and international collaborative efforts studying additional tissue types, different deformation domains and common approaches to medical modeling and simulation.

Addressing the perspective of national needs, and in particular those of the armed forces' medical personnel, this basic-level research provides a portion of the knowledge necessary to create better medical and surgical training technology for the medic through to the senior physician. More advanced simulation technologies are being developed both within this research group through other R&D efforts, and by numerous research and commercial groups around the world. Many of them will rely on the kind of data that we have produced, to ensure the realism and accuracy of their systems.

When one considers that the VA healthcare system treats not only combat-related injuries and conditions, but the normal medical needs of the members of the armed forces and their families, it is clear that any useful advance in basic medical technology will lead to better care. As quoted in the original proposal,

> "…military medical personnel have almost no chance during peacetime to practice battlefield trauma care skills. As a result, physicians both within and outside the Department of Defense believe that military medical personnel are not prepared to provide trauma care to severely injured soldiers in wartime…."
>
> [Bauer et al., 2000]

The kinds of training simulators enabled by this research can address the need to properly prepare medical personnel for the conditions that they will face both in the field and in the operating room.

For the future, we expect to continue this research with follow-on funding from sources including the ones listed above. Immediate applications of the data collected so far include: creation of improved polymer-based materials to create physical simulators that feel more realistic to the trainees; implementation of the models into the SOFA system so that the national and international partners can improve their models of various organ systems; and disseminating a "recipe book" detailing the process for adapting the technology and models developed here to researchers studying other tissues and organ systems.

References

[Bauer et al., 2000]

Bauer JJ, Magee JH, Moses G, Leitch, Dawson SL. Medical Simulation Training Initiative (MSTI). *Proceedings of SPIE*. 4037: 254-263, 2000

[Jordan & Howe, 2005]

Jordan P, Howe RD. Identifying the Parameters of a Nonlinear Constitutive Law for Soft Tissue Using Three-Dimensional Ultrasound Imaging. HST Forum, Boston, MA. (poster presentation)

[Kerdok, Ottensmeyer & Howe, 2006]

Kerdok AE, Ottensmeyer MP, Howe RD. The Effects of Perfusion on the Viscoelastic Characteristics of Liver, Journal of Biomechanics, 39, 2221-2231, 2006.

Appendices

Appendix A Kerdok Thesis - Chapter 4 & Appendix B

Chapter 4

Nonlinear Physically-Based Constitutive Model and Parameter Identification

The mechanics of a material are governed by the behavior of its constituents. A constitutive relation determines the state of stress at any point in a body in response to any arbitrary history of motion (Holzapfel 2000). Knowing the structure and the constitutive relationships that describe the material behavior of a composite body (i.e. an intact organ), the response of the body to any prescribed loading condition (i.e. surgical manipulations) can be obtained. The challenge is to define constitutive relations that are both simple enough to be easily implemented and realistic enough to accurately describe the material's behavior across different loading conditions. Currently, the lack of elegant and robust constitutive relations for soft biological tissues hinders the development of predictive biomechanics necessary for medical simulation (Fung 1993; Humphrey 2002).

Humphrey proposes a five-step procedure for developing a constitutive relation (Humphrey 2002):

1. Determine the general characteristics of interest
2. Establish a theoretical framework
3. Identify the specific functional forms of the constitutive relations
4. Calculate the values of the material parameters
5. Evaluate the predictive capability of the final relation

The results and analysis of the data presented in Chapters 2 and 3 summarize the general mechanical behavior of the liver. The nonlinear, viscoelastic, strain-rate dependent response to large deformations was found to be sensitive to its geometric and physiologic boundary conditions. These results are used to identify the functional form of the constitutive relations under the theoretical framework of continuum mechanics. The finite element method is used to solve the inverse boundary value problem. An iterative approach minimizes a prescribed objective function to identify the material parameters of the model from the multiple ramp indentation and stress relaxation data. Finally, the predictive capability of the model and its parameters are validated using stress relaxation, multiple ramp indentation, and the creep indentation data.

4.1 Physiologically Derived Constitutive Model

In Chapter 3 the liver was described as being mainly comprised of a tough collagenous capsule, vast cellular parenchyma, and pressurized fluid-filled vessels. In this chapter, the contribution of each of these constituents is accounted for while developing a model that allows for the cooperative nature of the tissue response.

The multi-physics based continuum model developed here relies on the previous modeling work of other soft tissue researchers. Socrate and Boyce developed a similar model for the large strain behavior of articular cartilage (2001). Febvey further developed their model to describe the mechanics of cervical stroma (2003). Both of these solid soft tissue structures were modeled as hyperelastic collagen and viscoelastic proteoglycan networks in parallel with a pressurized interstitial fluid network. Using a similar approach, the liver is modeled as a homogenous, initially isotropic, fluid-filled structure, containing a hyperelastic collagen network in series with a viscoelastic cellular network. A third porous network represents the volumetric response due to the fluid flow. Finally, the tough outer capsule structure is modeled as a hyperelastic collagenous membrane similar to Prevost's treatment of the chorioamnion (fetal membrane sac) (2006).

4.1.1 Motivation

The extracellular matrix (ECM) of soft tissues regulates the cell's shape, orientation, movement, and overall function (Park and Lakes 1992). ECM is comprised of elastin and collagen proteins in a hydrated ground substance. Elastin is considered the most linearly elastic biosoild with a Young's modulus of 0.6 MPa at 100% stretch (Park and Lakes 1992). Elastin is a long, flexible, cross-linked molecule whose molecular configuration changes with stretch. Collagen is the basic structural element in all tissues, with wavy fibers acting as mechanical units that dominate the force-stretch response. The initially compliant fibers stretch and reorient under a tensile load producing a nonlinear stiffening response with increased levels of stretch (Fung 1993; Liu and Bilston 2000).

Holzapfel suggests that soft biological tissues and solid polymers are unique in that they are the only materials that experience a nonlinear mechanical response to finite strains relative to an equilibrium state (2000). Since the polymer chain networks mimic the assembly of the wavy cross-linked collagen, the model used to describe the behavior of collagen is derived from models used in rubber elasticity. In particular, the 3D network model first described by Arruda and Boyce (1993) was used to describe the collagen in the parenchyma, and a 2D version of this model, proposed by Prevost, was used to represent the capsule (2006).

The ground substance of the ECM, and the cellular content of soft tissues, resist compressive forces, and maintain tissue structure. Under a compressive force, these molecules rearrange to produce a time-dependent viscoelastic response. Therefore, a model with a spring (to provide a back-stress) in parallel with a viscous component (to account for the time-dependant viscous shear relaxation) was used.

Lastly, the extracellular fluid in the liver (blood, bile, lymph, etc.) was accounted for by treating the liver like a fluid-filled elastic sponge. Using biphasic mixture theory, the fluid component responds to local changes in volume by creating a dynamic pressure term allowing for fluid flow within a porous elastic network. This flow in turn provides resistance to changes in volume with load over time. The solid component was

represented by an elastic spring whose bulk modulus contributes to changes in volume by resisting the flow from the fluid. This component works with the other elastic components described above to establish the equilibrium state of the tissue.

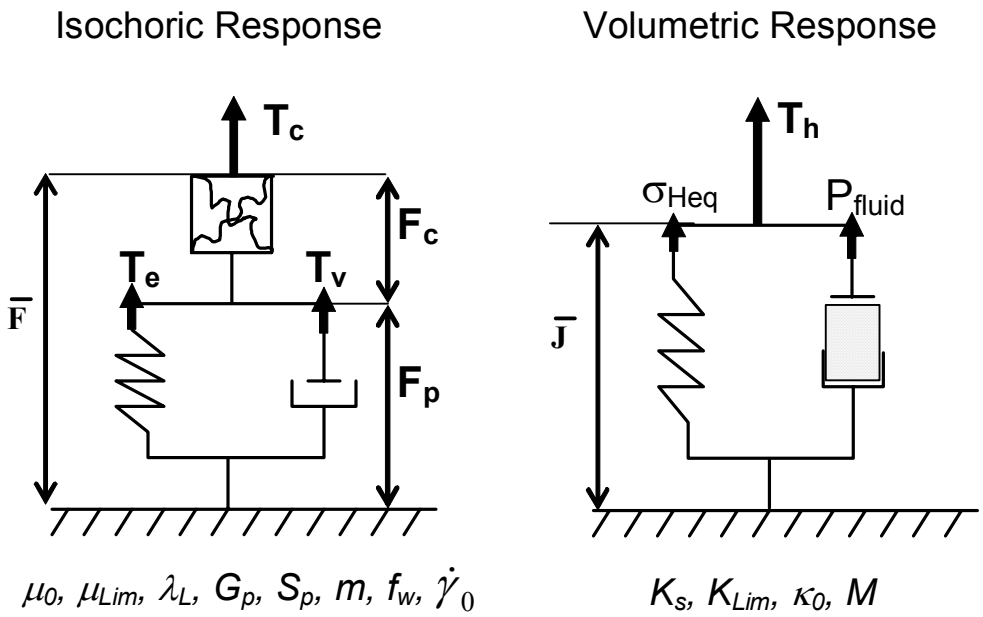

Figure 4.1 Rheological representation of constituve model sperated into the isochoric (deviatoric) response and volumetric (hydrostatic) response. Material parameters for the model elements are listed below the respective figure.

4.2 Constitutive Framework

The constitutive relation chosen to describe the liver is separated into its isochoric and volumetric components and can be represented by the rheological model in Figure 4.1. The total stress response of the tissue ($\boldsymbol{T}_{tissue}$) under an imposed deformation ($\boldsymbol{F}$) can be obtained by summing the deviatoric ($\boldsymbol{T}_{iso}$) and hydrostatic ($\boldsymbol{T}_h$) stresses that arise from the isochoric and volumetric component responses respectively

$$\boldsymbol{T}_{tissue} = \boldsymbol{T}_{iso} + \boldsymbol{T}_h . \tag{4.1}$$

As can be seen in Figure 4.1, the total deformation gradient tensor **F** is decomposed into its isochoric component $\bar{\mathbf{F}}$ and its volumetric component $J^{1/3}\underline{\boldsymbol{1}}$ (where $\underline{\boldsymbol{1}}$ is the identity tensor) and can be defined as:

$$\boldsymbol{F} = J^{1/3}\underline{\boldsymbol{1}}\bar{\boldsymbol{F}} \tag{4.2}$$

where J is the scalar volumetric Jacobian defined as the current volume (V) divided by the initial volume (V_0), and satisfies the condition: $det\left(\overline{\boldsymbol{F}}\right)=1$.

4.2.1 Isochoric Network

Consider a multiplicative decomposition for the isochoric deformation where

$$\overline{\boldsymbol{F}} = \boldsymbol{F}_c \boldsymbol{F}_p \,. \tag{4.3}$$

The collagen responds to the $\boldsymbol{F}_c$ component of the deformation gradient, while the $\boldsymbol{F}_p$ component is accommodated by the parenchyma through a dissipative constitutive response. A representation of the finite strain kinematics of this network is shown in Figure 4.2. $\boldsymbol{F}_p$ can be further decomposed into a left stretch tensor ($\boldsymbol{V}_p$) and a rotation tensor ($\boldsymbol{R}_p$) so that

$$\boldsymbol{F}_p = \boldsymbol{V}_p \boldsymbol{R}_p \tag{4.4}$$

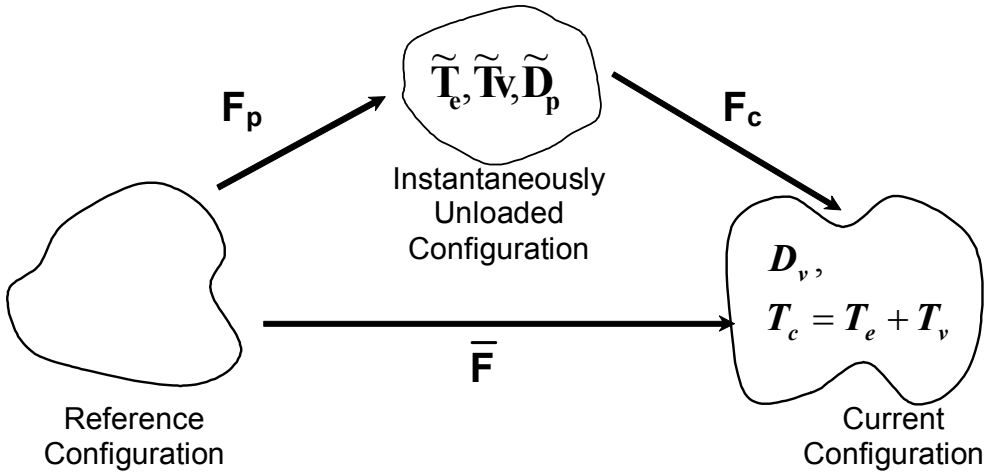

Figure 4.2 Finite strain kinematics for collagen network.

4.2.1.1 3D Hyperelastic Collagenous Component

The formulation of the hyperelastic collagen component of the constitutive relation relies on the 8-chain network model proposed by Boyce and Arruda (2000). This formulation uses a statistical model to represent the entropic state of the individual polymer chains in a network. A complete derivation of the model, as well as comparisons to other such models, can be found in (Arruda and Boyce 1993; Boyce and Arruda 2000). Although the Arruda-Boyce model is derived from an entropic understanding, it has also been successfully used to represent the nonlinear response of biological networks where the elastic response is controlled by the internal energy (Bischoff, et al. 1999). The force-stretch relationship can be defined for the individual fibrils of the collagen network by:

$$f_{fibril} = \frac{K_i}{b} L^{-1}\left(\frac{\lambda_f}{\lambda_L}\right) \tag{4.5}$$

where K_i is a reference stiffness, b is the persistence length for the fibril, λ_f and λ_L are the current stretch and locking stretch of the collagen fibril, respectively. L^{-1} is the inverse Langevin function defined by (Kuhn and Gruhn 1942):

$$\beta = L^{-1}\left(\frac{\lambda_f}{\lambda_L}\right), \text{ where} \tag{4.6}$$

$$L(\beta) = \coth\beta - \frac{1}{\beta}. \tag{4.7}$$

A simple representative cubic unit structure defines the geometry of the 8-chain network such that the response of a single chain (fibril) can be linked to the global deformation of the network due to symmetry (Figure 4.3).

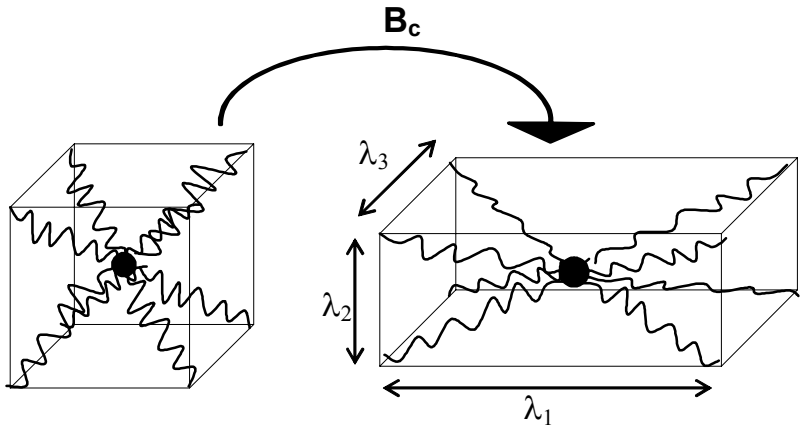

Figure 4.3 The 8-fibril collagen network unit cell and principal stretches under deformation.

The unit cell deforms with the principal stretches, while the junction point remains centered, allowing the stretch in each fibril to be shared equally amongst all of the others via

$$\lambda_f = \sqrt{\frac{\lambda_1^2 + \lambda_2^2 + \lambda_3^2}{3}}. \tag{4.8}$$

In addition to experiencing the same stretch, each fibril also rotates towards the direction of highest stretch.

The Cauchy stress exerted by the collagen network is obtained in terms stretching a collagen fibril by the left Cauchy-Green stretch tensor ($\boldsymbol{B}_c$)

$$\boldsymbol{B}_c = \boldsymbol{F}_c \boldsymbol{F}_c^T \tag{4.9}$$

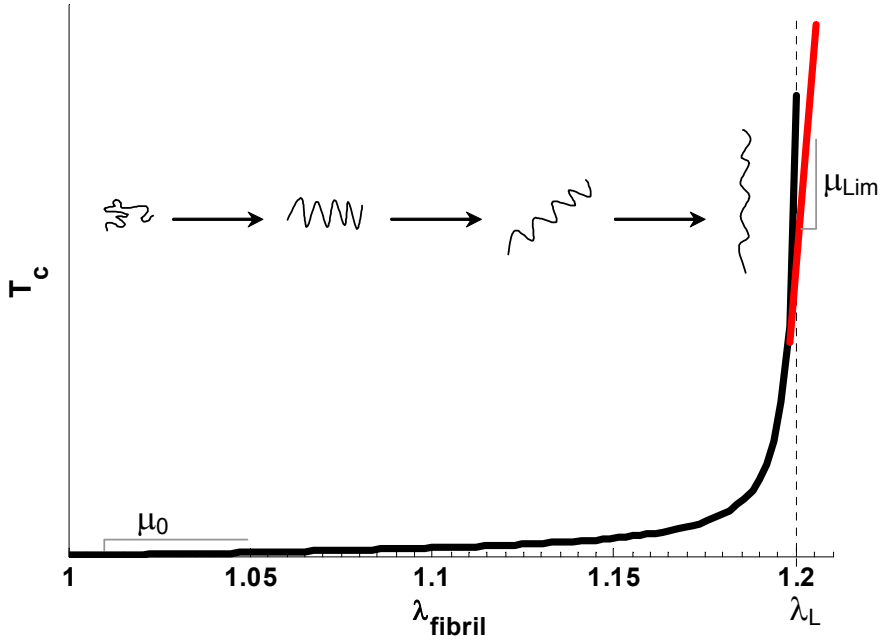

Figure 4.4 A representative stress-stretch response of the collagen netork highlighting a respone of a single fibril, the initial and limiting shear moduli, and the locking stretch.

through the following constitutive law

$$\boldsymbol{T}_c = \frac{1}{J}\left(\mu_0\left(\frac{\lambda_L}{\lambda_f}\right)\beta\left(\boldsymbol{B}_c - \lambda_f^2\,\underline{\boldsymbol{1}}\right)\right) \tag{4.10}$$

where the initial shear modulus (μ_0) and the fibril locking stretch (λ_L) are the material parameters. The stress-stretch response for this relation, and a depiction of the fiber orientation is shown in Figure 4.4. Since tissues cannot experience infinite stress, and are capable of stretches beyond the locking stretch, the slope of the stress-stretch response near the locking stretch (0.995 λ_L) is used to define a limiting shear modulus (μ_{Lim}).

The collagen stress is considered to be purely deviatoric (tr $\boldsymbol{T}_c$=0): the collagen is not allowed to account for any of the volume changes seen in the overall tissue response. This "split" approach was taken due to the observation that the majority of the volume change in liver is due to the movement of the extracellular fluid, rather than taken up by the stretch of the collagen (Figure 4.5). An initial trial allowing the collagen to account for changes in volume proved problematic as the volumetric too dominant. The split approach also has the advantage of easier parameter identification through simplified initial calculations.

4.2.1.2 Viscoelastic Parenchyma Component

A portion of the deviatoric Cauchy stress ($\boldsymbol{T}_c$) derived above is balanced by the elastic back stress ($\boldsymbol{T}_e$) carried by the non-dissipative component of the parenchyma

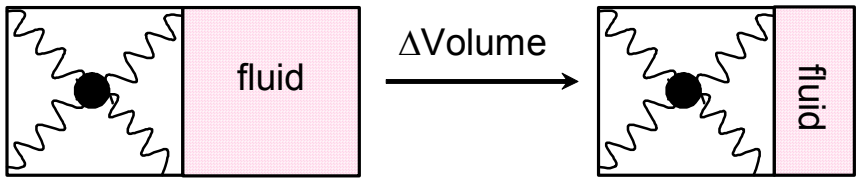

Figure 4.5 Representation of the assumption that the fluid component of the model takes up the majority of the change in volume.

network. The remainder of the stress ($\boldsymbol{T}_v$) drives the evolution of the viscous component of the deformations gradient,

$$\boldsymbol{T}_c = \boldsymbol{T}_e + \boldsymbol{T}_v . \tag{4.11}$$

The back stress element is modeled through a linear elastic constant shear modulus (G_p) so that the associated Cauchy stress is

$$\widetilde{\boldsymbol{T}}_e = \frac{1}{J}\left(2G_p \left[\boldsymbol{E}_p - \frac{tr\boldsymbol{E}_p}{3}\underline{\boldsymbol{1}} \right] \right). \tag{4.12}$$

Here $\boldsymbol{E}_p$ is the Hencky strain associated with the viscous stretch ($\boldsymbol{V}_p$): $\boldsymbol{E}_p = ln\boldsymbol{V}_p$**.** Since the definition of a isochoric response requires that the $\det(\overline{\boldsymbol{F}}) = \det(\boldsymbol{F}_c) = \det(\boldsymbol{F}_p) = 1$, and that the $\det(\boldsymbol{R}_p) = \det(\boldsymbol{V}_p) = 1$, the $\mathrm{tr}(\boldsymbol{E}_p)=0$ and the elastic back stress is reduced to

$$\widetilde{\boldsymbol{T}}_e = \frac{1}{J} 2G_p \boldsymbol{E}_p . \tag{4.13}$$

This response is again purely deviatoric, thus $\mathrm{tr}(\widetilde{\boldsymbol{T}}_e)=0$. $\widetilde{\boldsymbol{T}}_e$ is defined in the instantaneously-unloaded configuration. To properly prescribe the evolution of the viscous deformation, the back stress needs to be pushed forward to the current configuration by,

$$\boldsymbol{T}_e = \frac{1}{J} \boldsymbol{F}_c \widetilde{\boldsymbol{T}}_e \boldsymbol{F}_c^T . \tag{4.14}$$

The deviatoric driving stress for the viscous deformation ($\widetilde{\boldsymbol{T}}_v$) is obtained from

$$\boldsymbol{T}_v = \boldsymbol{T}_c - \boldsymbol{T}_e \tag{4.15}$$

The magnitude (τ) and direction ($\boldsymbol{N}$) of the deviator of the viscous stress are defined as:

$$\boldsymbol{N} = \frac{\boldsymbol{T}_v'}{\|\boldsymbol{T}_v'\|} = \frac{\boldsymbol{T}_v'}{\sqrt{2\tau}}, \text{ where} \tag{4.16}$$

$$\mathbf{T}'_{\mathrm{v}} = \mathbf{T}_{\mathrm{v}} - \frac{1}{3}\mathbf{tr}\mathbf{T}_{\mathrm{v}}\underline{\mathbf{1}} \tag{4.17}$$

The viscous stretching tensor ($\boldsymbol{D}_p$) is constitutively prescribed to be parallel to the deviator of the viscous stress ($\boldsymbol{T}'_v$) through

$$\boldsymbol{D}_p = \dot{\gamma}^v \boldsymbol{N} \tag{4.18}$$

where the viscous shear strain-rate $\dot{\gamma}^v$ depends on a power law relationship through the magnitude of the driving stress (τ) and on material parameters S_p (shear strength modulus) and m,

$$\dot{\gamma}^v = \dot{\gamma}_0^v \left(\frac{\tau}{S_p} \right)^m . \tag{4.19}$$

For m = 1, this relationship reduces to a linear viscous response. For m>1 this relationship can be used to account for the effect of thermally activated processes.

The rate of change of the viscous component of the deformation ($\dot{\boldsymbol{F}}_p$) can be expressed as

$$\dot{\boldsymbol{F}}_p = \widetilde{\boldsymbol{L}}_p \boldsymbol{F}_p \tag{4.20}$$

where $\widetilde{\boldsymbol{L}}_p$ is the viscous velocity gradient in the instantaneously-unloaded configuration and can be expressed as the sum of the stretching tensor ($\widetilde{\boldsymbol{D}}_p$) and spin tensor ($\widetilde{\boldsymbol{W}}_p$),

$$\widetilde{\boldsymbol{L}}_p = \widetilde{\boldsymbol{D}}_p + \widetilde{\boldsymbol{W}}_p . \tag{4.21}$$

The stretching tensor in the instantaneously-unloaded configuration is obtained by pulling back the viscous stretching tensor via

$$\widetilde{\boldsymbol{D}}_p = \boldsymbol{F}_c^{-1} \boldsymbol{D}_p \boldsymbol{F}_c . \tag{4.22}$$

The arbitrary rotation associated with the definition of the instantaneously-unloaded configuration is eliminated by setting $\widetilde{\boldsymbol{W}}_p$=0.

The stress from the isochoric network ($\boldsymbol{T}_{iso}$) is therefore defined as the stress in the collagen network ($\boldsymbol{T}_c$), which is equal to the sum of the stresses from the elastic ($\boldsymbol{T}_e$) and viscous ($\boldsymbol{T}_v$) components of the parenchyma network ($\boldsymbol{T}_p$)

$$\boldsymbol{T}_{iso} = \boldsymbol{T}_c = \boldsymbol{T}_p = \boldsymbol{T}_e + \boldsymbol{T}_v . \tag{4.23}$$

4.2.2 Volumetric Network

There are two components to the liver response due to local changes in volume. One component considers an equilibrium response arising from the combined effect of osmotic pressure, volumetric elastic response of the solid matrix, perfusion pressure, and resistance to extracellular flow. The other component arises from the establishment of the non-equilibrium pressure gradient that drives the fluid flow through the tissue.

4.2.2.1 Equilibrium Response

A simplistic model of the liver is considered in which an initial volume fraction (f_w) can be associated with the amount of free fluid in the system. The remaining volume ($1\text{-}f_w$), represents the solid phase and its associated (bound) hydrated fluid tissue component. As long as the volumetric strain ($J\text{-}1$) is greater than f_w, an effective volumetric Jacobian (J^*) can be defined as

$$J^* = \frac{f_w - (J-1)}{f_w}. \tag{4.24}$$

The volumetric equilibrium stress response (Figure 4.6) is then simply expressed as

$$\sigma_{Heq} = K_s \ln(J^*) \tag{4.25}$$

where K_s is a constitutive parameter that relates to the small strain bulk modulus (K_0) through

$$K_s = K_0 f_w \tag{4.26}$$

As the volumetric strain approaches the limit of f_w, this formulation asymptotes to an infinite stress state. Under this condition it is important to recognize that the solid component (f_s) is not incompressible, and can be associated with a limiting bulk modulus K_{Lim}. The relationship between the hydrostatic equilibrium stress and the volumetric strain has therefore been formulated to have an asymptotic linear slope equal to K_{Lim}.

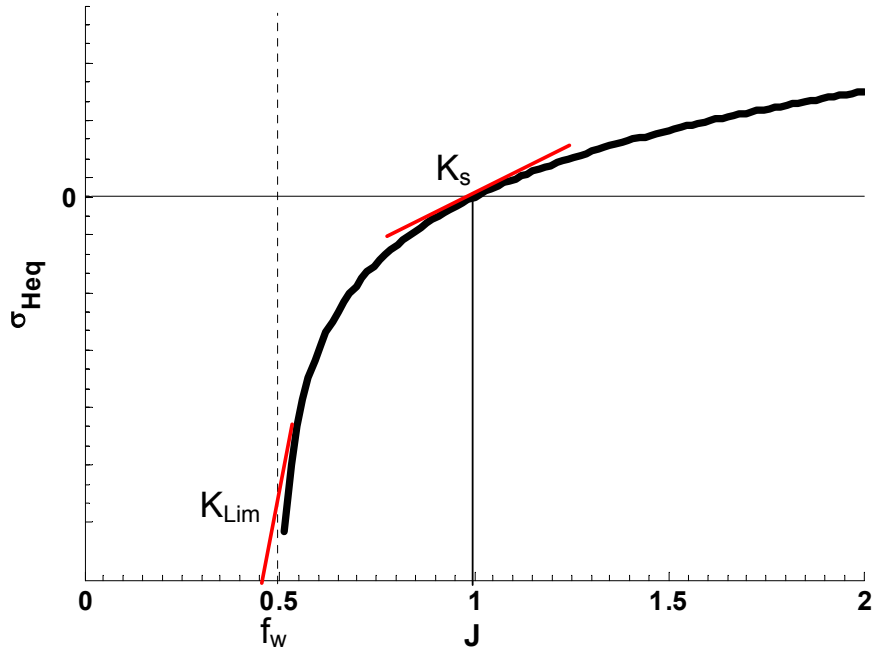

Figure 4.6 Representation of hydrostatic equilibrium stress versus the volume highlighting the equilibrium (K_s) and limiting (K_{Lim}) bulk moduli and the amount of free water (f_w).

4.2.2.2 Transient Response

Finally, the volumetric transient response is based on fluid flow through a porous medium as governed by a simple linear Darcy's Law,

$$q = -\kappa \nabla P_{fluid} \tag{4.27}$$

where q is the macroscopic volume flow rate, κ is Darcy's hydraulic permeability representing the resistance to flow under zero strain, and P_{fluid} is the dynamic fluid pressure. To account for variations in permeability with deformation, the permeability is considered to be a function of volumetric strain ($\varepsilon_V = J-1$) through the relationship given by (Ateshian, et al. 1997)

$$\kappa = \kappa_0 \left[\frac{\varphi_0 \varphi_f}{(1-\varphi_0)\varphi_s} \right]^2 e^{\frac{M\varepsilon_V}{2}} . \tag{4.28}$$

Here ϕ_s and ϕ_f are the respective solid and fluid contents of the tissue (where $\phi_s + \phi_f = 1$), κ_0 and ϕ_0 are the permeability and solid content of the tissue in the absence of volumetric strain, respectively, and M is the nonlinear permeability coefficient. κ_0 and M are material parameters for finite deformations.

The time dependent fluid-pressure in the tissue can be obtained by solving the following equation at each material point over the liver domain

$$\left[\frac{1}{K_{Lim}}\right]\dot{P}_{fluid} = \kappa\nabla^2 P_{fluid} - \frac{\dot{J}}{J}. \tag{4.29}$$

The volumetric stress response ($\boldsymbol{T_h}$) is therefore represented as the sum of the contributions from the hydrostatic equilibrium response (σ_{Heq}) and the transient fluid pressure response (P_{fluid}),

$$\boldsymbol{T_h} = \sigma_{\boldsymbol{Heq}}\,\underline{\boldsymbol{1}} - P_{\boldsymbol{fluid}}\,\underline{\boldsymbol{1}}. \tag{4.30}$$

4.2.3 Hyperelastic 2D Collagenous Capsule

The liver capsule was modeled as a 2D representation of the 3D hyperelastic collagen network. This work relies on the previous modeling work of Prevost, who modeled the human chorioamnion as an "idealized" continuum membrane whose in-plane response is dominated by the collagen fiber network (Prevost 2006). A four-fibril network is used as the unit cell, and in this case the collagen network is allowed to respond to changes in area. Hence in addition to the locking stretch λ_{LCap}, initial (μ_{0Cap}) and limiting shear moduli (μ_{LimCap}), and area expansion modulus (K_{Cap}) is also required as a material parameter. The Cauchy membrane stress is given by,

$$\boldsymbol{T_{Cap}} = \frac{\mu_{0Cap}\lambda_{LCap}}{J}\left[\frac{\beta}{\lambda_{\boldsymbol{LCap}}}\boldsymbol{B_{cap}} - \beta_0\,\underline{\boldsymbol{1}}_{\boldsymbol{2D}}\right] + K_{Cap}(J-1)\underline{\boldsymbol{1}}_{\boldsymbol{2D}} \tag{4.31}$$

where $\boldsymbol{B_{cap}}$ is the 2D left Cauchy-Green stretch tensor, and β_0 is the inverse Langevin function of ($1/\lambda_{Lcap}$). For the capsule, the limiting shear modulus was defined by its critical stretch (λ_{linear}). This stretch is the point beyond which the network starts responding with a linear force-stretch relationship

4.3 Physical Interpretation of Framework in Relation to Observed Experimental Response

The constitutive framework for the response of liver tissue outlined in sections 4.6.1 and 4.6.2 resulted in a model for the liver where the total stress response from an imposed deformation is a sum of the contributions from the isochoric and volumetric responses

$$\boldsymbol{T_{tissue}} = \boldsymbol{T_c} + \sigma_{\boldsymbol{Heq}}\,\underline{\boldsymbol{1}} - P_{\boldsymbol{fluid}}\,\underline{\boldsymbol{1}}. \tag{4.32}$$

To understand the physical meaning that correlates the biologically relevant material parameters to the proposed constitutive framework, the model's response to a step deformation is considered. The instantaneous ($t = 0^+$), long term ($t\rightarrow\infty$), and transient ($0 < t < \infty$) responses for different modes of deformation (change in volume, pure shear, and indentation) are discussed.

An instantaneous change in volume gives rise to very large hydrostatic stresses because K_{Lim} dominates the instantaneous bulk modulus. Since most biological tissues

have a high water content (~70%), the modulus is expected to be similar to those of incompressible materials, having the same order of magnitude as that of water (2.2 GPa).

Instantaneous changes in shape (shear or isochoric deformations) are accounted for by an immediate shear response controlled by the hyperelastic collagen network. The collagen network provides the nonlinear "stiffening" character of the tissue response (Figure 4.4). At low levels of stretch, the curve has an initially flat response described by a low initial shear modulus (μ_0). The response then sharply increases with stretch as the limiting stretched is approached before becoming linear again with a modulus much larger than the initial shear modulus (μ_{Lim}). For a nonhomogenous mode of deformation, like indentation, the material should behave in a nearly incompressible manner since K_{Lim} is much greater than the hyperelastic shear moduli ($\mu_{0,}\ \mu_{Lim}$).

The dissipative mechanisms are recruited when a constant level of deformation is held over time. These elements are responsible for a portion of the imposed deformation. At long times ($t\rightarrow\infty$), the material reaches an equilibrium steady-state in which the response to changes in volume is controlled solely by the equilibrium bulk modulus (K_s). The response to change in shape is accommodated by both the hyperelastic collagen network and the reconfiguration of the viscoelastic parenchymal structure. This is portrayed through a series combination of the collagen moduli and a lower shear parenchyma modulus (G_p).

The transient response of the material is accounted for by the material properties of the dissipative components of the model. The characteristic time for changes in volume is controlled by the permeability (κ) and the length-scale associated with the diffusion paths. For a linear poroelastic model of a tissue specimen of height l in confined compression, this time can be defined by,

$$\tau_{vol} = \frac{l^2}{H\kappa}, \tag{4.33}$$

where H is the confined compression modulus. In the case where the elastic response of the material is nonlinear, κ is an exponential function of volume, and the diffusion paths are 3D (recall the complicated structure of the liver vasculature and its hexagonal lobule comprised of longitudinal portal veins, hepatic arteries, bile ducts, and central veins and densely packed transversely oriented fenestrated sinusoids). Therefore, the relationship of the volumetric time constant (τ_{vol}) presented in Equation 4.33 is an over simplification. However, it does provide the correct dimensional framework to begin to interpret the experimental data. Note that the size dependency of this model feature cannot be replaced by a simple viscoelastic formulation since no length-dependant behavior of the tissue response is possible with viscoelastic models.

Lastly, the material's transient isochoric response is described by the nonlinear viscous element shown in Equation 4.19. This relationship is graphically depicted in Figure 4.7. A linear response is obtained for m=1. As the value of m is increased, the strain-rate dependence diminishes, and the material is allowed to flow easily at high rates when the driving stress (τ) exceeds the material strength (S_p). These strain-rate independent behaviors are more indicative of biological materials, where it has been shown that hysteresis is constant over a wide variety of strain-rates (Fung 1993), and where the tissue is filled with blood, a non-Newtonian fluid.

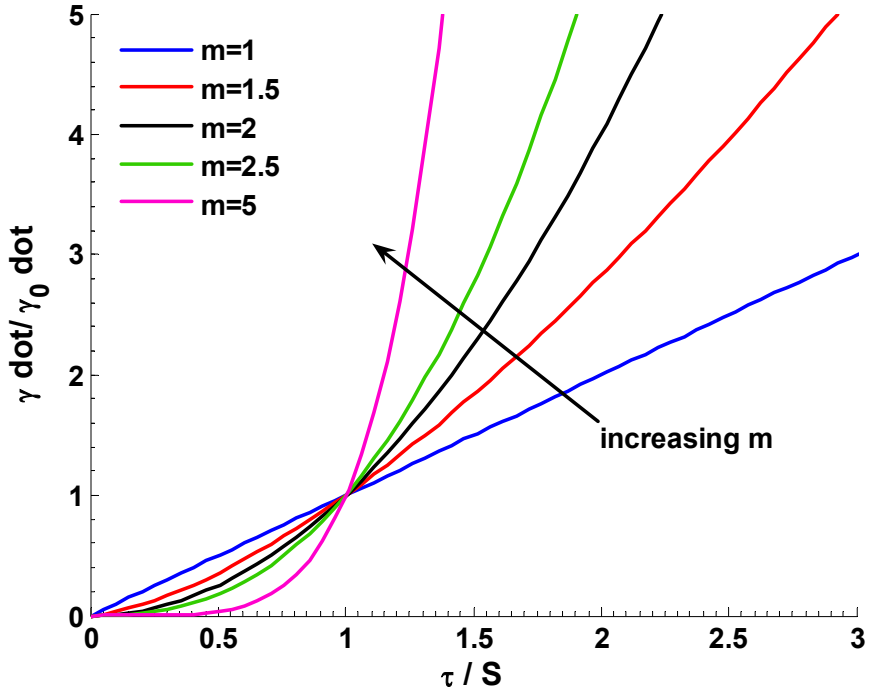

Figure 4.7 The effects of changing *m* on the stress response of the parenchyma viscous network.

4.3.1 Material Parameter Estimation

The preceding sections sought to define an appropriate constitutive model and its physiologically based parameters to appropriately depict the mechanical response of liver to finite deformations. Before implementing an iterative numerical approximation scheme to realize the values of these parameters, an ad hoc approach to determine reasonable start values for the parameters is presented based on the literature, and features from the experimental data.

- K_{Lim} is set to 0.22 GPa based on the high strain-rate dynamic testing reported by Saraf et al. (Saraf, et al. 2005)
- μ_0 is bounded based on the initial slopes of the ramp indentation tests (1-100 Pa)
- μ_{Lim} is set based on the initial slope of the unloading curves during ramp indentation testing. The rapid change in direction of the displacement is mainly accounted for by the unloading of the hyperelastic network. This value was set to 1.5 MPa based on experimental indentation data.
- λ_L is bounded based on the curvature of the ramp indentation data. Observing where the response turned nonlinear approximated the locking stretch asymptote (1.01-1.2). The force-displacement response of the model is extremely sensitive to this parameter as it drives the nonlinear loading response, effects the peak force, and dominates the initial unloading response (where μ_{Lim} is set).

- f_w is determined given the typical mass of the liver (1.1-1.7 kg) and the amount and densities of free fluid (namely blood, bile, and lymph) stored within the organ at any time. Given values from the literature, the fraction of free fluid in the liver was determined to be 50-70% of it's mass, and f_w was set to 0.5 (Gray 1977).
- G_p was found to be rather insensitive to ramp indentation tests. Instead the stress relaxation data was used. Knowing that $K_{Lim} >> \mu_{Lim} >> G_p$, this elastic shear modulus was determined such that an appropriate steady-state stress relaxation response was achieved (10-25,000 Pa).
- K_s was determined based on the peak force of indentation ramp tests, the stress relaxation steady-state response and curvature, and an independent test conducted where the mass of the liver was measured over time after a step increase in perfusion pressure. Prior to indentation testing, a harvested liver from an 81 kg pig was allowed to perfuse for 45 minutes in the *ex vivo* perfusion system following the protocol in Chapter 3. The liver was placed on a digital scale and the IVC was cannulated so that the liver could drain elsewhere. The hepatic arterial perfusion was clamped (to ease the control of the outflow) and the portal venous pressure was quickly raised 76 mm inducing a step change in pressure (dP) of 0.75 kPa. The mass of the liver was recorded over time and converted to volume (dV) (Figure 4.8). This procedure was repeated twice. The results were fit to a decaying exponential whose constants (V_{eq} and τ_{perf}) were determined by minimizing the mean square error and the derivative of the response to the model,

$$dV = V_{eq}(1 - e^{-\frac{t}{\tau_{perf}}}). \tag{4.34}$$

  V_{eq} was found to be 3.614×10^{-5} and 5.123×10^{-5} m^3 for the two tests with τ_{perf}'s of 32.1 and 44.54 seconds respectively. K_s was then estimated using

$$K_s = \frac{dP}{dV} V_0, \tag{4.35}$$

  where V_0 was the initial volume of the liver prior to the step change in pressure. The results suggest an equilibrium bulk modulus of 37-59 kPa. Since the other elastic moduli in the model are also likely resisting the change in volume, and recalling that K_s is related to the amount of free water in the organ, K_s was bounded to be between 1 and 50 kPa.

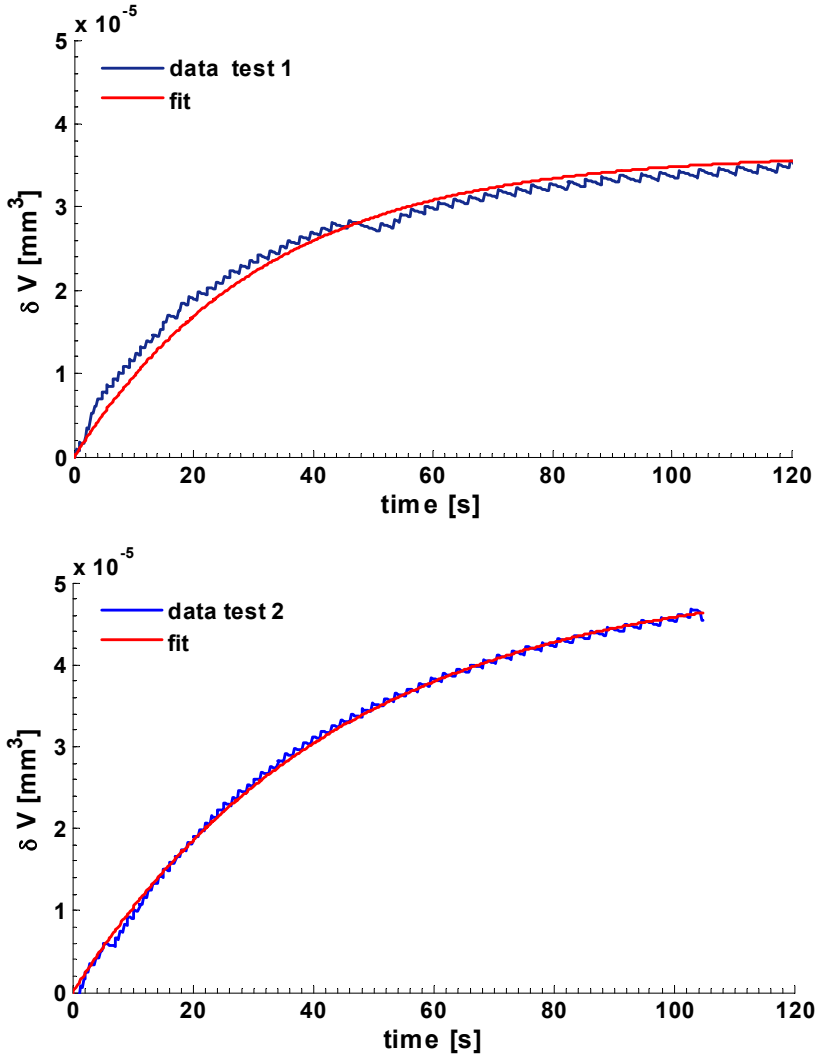

Figure 4.8 Change in volume over time data from filling test to determine start values for κ_0.

- κ_0 was also estimated from the results of the swell test. Solving Equation 4.31 for κ_0,

$$\kappa_0 = \frac{l^2}{K_s \tau_{perf}}, \tag{4.36}$$

using K_s as the moduli, assuming a length-scale equal to ½ the length of one of the liver lobules (~0.1 m), and using the results of the fit for τ_{perf}, initial estimates for κ were found to be between $5.8\text{x}10^{-9}$ and $6\text{x}10^{-9}$ m^4/Ns. Looking at the response of the model to changes in κ (namely peak force and amount of hysteresis in the ramp indentation tests) suggests that κ can range between $1\text{x}10^{-6}$ and $10\text{x}10^{-9}$ m^4/Ns.

- M was determined from the results of the uniaxial confined compression tests done on cartilage by Ateshian et al (1997). They showed that M ranges from 0.4 to 4.3, and that κ changes by 10% when M changes by > 100%. Given the nonhomogenous

indentation tests, and this insensitivity of M on the response, M was set to 4 assuming that liver would fall on the higher end of values for cartilage.

- $\dot{\gamma}_0^v$ was set to 0.01. Since the parameter for the viscoelastic parenchyma network can be represented by $\frac{\dot{\gamma}_0^v}{S_p^m}$, the initial shear rate was set so that flow would occur at 1% strain/second when the driving stress was equal to the shear strength (S_p).
- S_p and m affect the strength of the viscous response from the parenchyma network. This network is assumed to be responsible for the slower time constant of the response. Therefore, the stress relaxation data was used to determine these material parameters. S_p affected both the steady-state stress level as well as the curvature of the response, whereas m drastically affected the curvature of the response. Higher *m's* resulted in a steeper initial stress relaxation. The value of m was set for each liver using the stress relaxation tests, and checked in the multiple rate ramp indentation tests to ensure that hysteresis remained consistent with rate. Since the response was more sensitive to m than S_p, the range of m was set from 1.1-10, and S_p was more loosely bounded to be between 0.1-100 kPa.

In summary, the 12-parameter physically-based constitutive model presented in this section can be reduced to five dependent material parameters (K_{Lim}, μ_{Lim}, $\dot{\gamma}_0^v$, f_w, M), and seven independent material parameters (μ_0, λ_L, K_s, G_p, S_p, m, κ_0). The identification of these seven material parameters is done through iterative inverse finite modeling and is discussed below.

4.4 Parameter Identification via Iterative Inverse FEM

4.4.1 Numerical Approximation of Constitutive Model

Although indentation testing lends itself well for obtaining the mechanical response of whole perfused livers to known forces and/or displacements, the interpretation of the results is complicated, particularly under finite deformation. In addition, the constitutive relationship defined in the preceding section (Equation 4.32 from Equations 4.10, 4.14, 4.19, 4.25, and 4.30) cannot be analytically solved in a straightforward manner. The two components of stress giving rise to the deviatoric response ($\boldsymbol{T_c}$, $\boldsymbol{T_p}$) are entirely defined by solving the initial boundary value problem by following the evolution of the deformation gradient at each material point. The volumetric component can only be obtained by solving the diffusion equation at each material point over the entire domain. The resulting nonlinear multiphysics-based problem cannot be solved without the use of numerical approximation methods such as finite element modeling.

To solve the inverse problem (identifying the material parameters from the known force-displacement response), the model was implemented using commercial finite element software (ABAQUS version 6.5, Providence, RI). The constitutive equations describing the behavior of the 2D liver capsule and 3D tissue structure were coded as user defined materials (UMAT) in a subroutine. The implicit formulation of the time integration used in the subroutine is beyond the scope of this work, but details can be found in Appendix A of Febvay (2003). The implementation of the isochoric network is

straightforward. The diffusion equation however is realized to be analogous to a heat diffusion equation,

$$\rho c_p \dot{T} = \kappa_T \nabla^2 T + r_{gen}, \tag{4.37}$$

where ρ is the density, c_p is the specific heat, T is temperature, κ_T is the thermal conductivity, and r_{gen} is the heat source term. The local equation for the time evolution of the fluid pressure is therefore treated as a coupled thermal-mechanical problem.

4.4.2 Inverse Finite Element Modeling

Solving the inverse problem requires replication of the experimental boundary conditions in the form of a finite element model (Figure 4.9). Either the force or the displacement data are used as prescribed inputs to the model. The constitutive relation and its material parameters govern the model's response to the prescribed loading condition. Initial estimates are given to the material parameters and an error estimate between the model's response and the experimental data is determined. The parameters are then updated in an iterative fashion until the model's result matches that of the data.

Given the length scale of the liver lobe (~250 x 130 mm) to the size of the indenter (6-12 mm diameter), the indentation tests were represented with an axisymmetric geometry assuming an infinite half-space (Figure 4.10). The width (w) and height (h) of the mesh were changed according to the actual dimensions of the liver. The tissue was modeled as a homogenous, deformable, solid with 8-node, axisymmetric, thermally-coupled, quadrilateral, biquadratic, bilinear, temperature elements (CAX8T). The mesh was biased to have increased density in the area under the indenter, but kept as coarse as possible to increase computation time. Comparing the results from meshes with

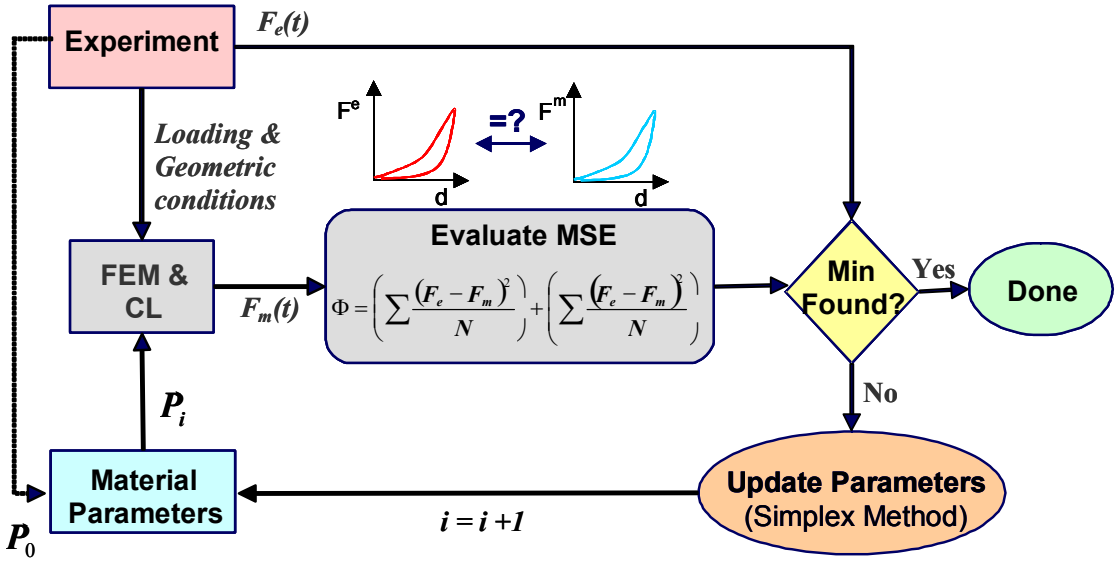

Figure 4.9 A schematic of the iterative algorithm used to solve the inverse problem with a finite element model (FEM).

10x finer resolution showed no noticeable change in reaction force. The total number of elements ranged from 147 to 160 depending on the size of the specimen, but each had a 6 mm x 12 mm area directly under the indenter with 47 elements.

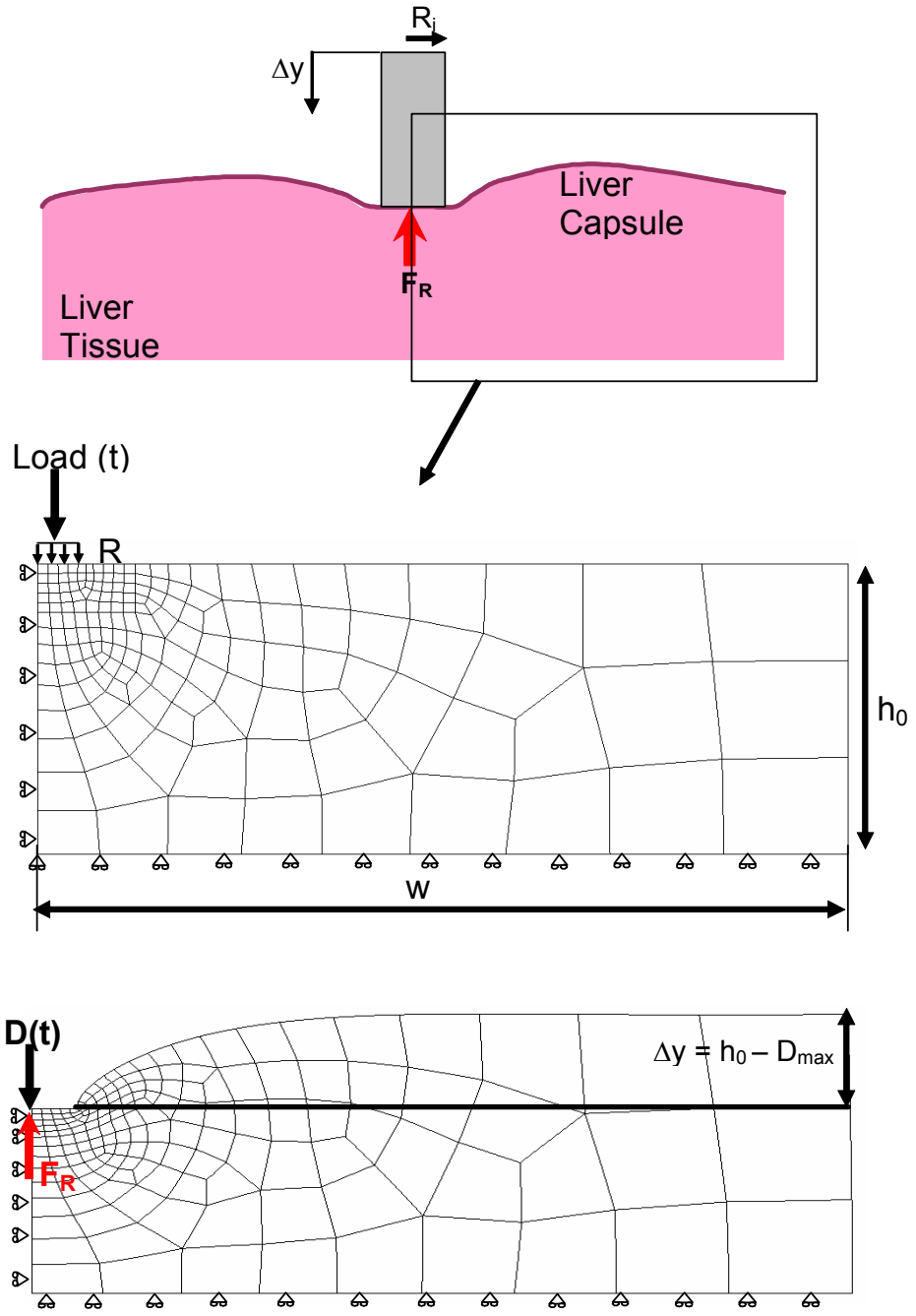

Figure 4.10 (Top) A schematic representation of the indentation experimental conditions. Middle) The axisymmetric meshed geometry and boundary conditions used in ABAQUS to represent the experimental conditions. (Bottom) An example of a deformed mesh showing the reaction force on the indented area.

The capsule was modeled as a 100 μm thick homogenous shell using the skin feature in ABAQUS. The mesh was matched in number to the tissue below, with 3-noded quadratic axisymmetric thin-shelled elements (SAX2). An independent model was created to solve for the capsule parameters using the uniaxial tension experiments. The user defined material for capsule required that an axisymmetric condition be modeled. Therefore a tube in uniaxial loading approximated a thin sheet in confined uniaxial tension, and a correction factor for the force was used to relate their areas

$$F_{cap} = \frac{F_{model}}{0.99\pi} \ . \tag{4.38}$$

Twenty, 2-node, linear, axisymmetric, thin-shelled, elements (SAX1) 100 μm thick were used to model the capsule. The bottom of the capsule model was held fixed, the top was constricted to vertical motions, and the displacement history from the data was used for the loading condition.

Since the motorized indentation tests used a suction indenter, the complete liver model was deformed by directly displacing the nodes equal to the radius of the indenter. The reaction force was taken from a master node constrained to the load nodes. A 12 mm diameter discrete, analytical, rigid, indenter with a fillet radius of 0.4 mm, was also created and the contact problem solved by allowing a no-slip condition (tangential friction set to 0.9) under the area of the indenter, and a frictionless condition on the corners. Normal contact was defined using an augmented Lagrange "Hard" contact pressure-overclosure for the no-slip area, and an exponential pressure-overclosure for the frictionless section with pressure equal to 1e6 Pa and a clearance of 4e-5 m. There were minimal differences seen in the force responses from the model with direct indentation to the one using the indenter. Therefore, the direct indention was used since it greatly decreased computation time. The 6 mm diameter indenter for the creep experiment was modeled, however, and a frictionless condition like the one described above was used.

The displacement data from the motorized indentation experiments were directly implemented into the loading conditions for the model using the AMPLITUDE feature in ABAQUS. The displacement history was applied to the master node, while the reaction force was recorded. For the creep tests, an initial displacement was imposed on the indenter to simulate the inertial loading of the dropped mass (~20% nominal strain in 0.1 sec), and then a –0.3188 N load was maintained for the duration of the test. In all cases the bottom of the tissue was allowed to slip in the transverse direction. Lastly, the temperature was initially set to be 0 everywhere, and then was inactivated to resemble a pressurized tissue covered in a non-permeable membrane.

4.4.3 Optimization Technique

The seven-dimensional parameter space of the constitutive model was systematically explored and the results compared to the data using an optimization scheme. A link between Matlab (version 7 R14, Mathworks Inc, Natick, MA) and ABAQUS environments carried out an iterative adjustment of the material parameters according to the Nedler-Mead simplex method (Jordan, et al. 2005a; Lagarias, et al. 1998). The objective function (Φ) to be minimized was defined using the mean square error between

the data and the model of the force versus displacement (or time in the case of multiple indentations) curve and the time derivative of that curve

$$\Phi = \left(\sum \frac{\left(\boldsymbol{F}_{data} - \boldsymbol{F}_{model} \right)^2}{\boldsymbol{n}} \right) + \left(\sum \frac{\left(\dot{\boldsymbol{F}}_{data} - \dot{\boldsymbol{F}}_{model} \right)^2}{\boldsymbol{n}} \right) \tag{4.39}$$

The simplex was allowed to only sample the solution space within the bounds given for each parameter, and convergence was highly sensitive to the initial parameter estimation. Convergence, or termination, conditions were set to either a maximum of 1,000 iterations, or a normalized simplex diameter less than 1×10^4. If a numerical solution was not possible, and the model "crashed", an large error (~100) was returned and the iterations continued. An iterative solution for a single indentation consisting of 200 iterations required approximately 10 hours of computation time on a 3.0 GHz Pentium 4 machine with 2 GB of RAM.

4.5 Results

4.5.1 Uniaxial Capsule Tests

The optimization scheme was first tried for the 4-parameter membrane constitutive model (Equation 4.31) on the capsule uniaxial tension tests. Initial values for the material parameters (μ_{0Cap}, λ_{LCap}, λ_{linear}, K_{Cap}) were estimated by manually fitting the models response to the data. The optimization was then run for each of the 9 tests until a minimum was found (mean MSE = 0.00184 in 195-595 iterations). The results for the parameters are shown in Table 4.1, and the mean results are plotted against the data for each test in Figure 4.11.

The mean and standard deviation of the results suggest that the model was more sensitive to changes in the stretch parameters than the shear and bulk moduli. The model response is in excellent agreement with the data. The combined values for the parameters were used in the indentation testing models below.

Table 4.1 The optimized material parameters for the liver capsule from uniaxial tension testing

	λ_{linear}	λ_{LCap}	μ_{0Cap} [Pa]	K_{Cap} [MPa]	MSE
Test 1 Mean (SD)	1.023 (0.021)	1.040 (0.02)	7383.364 (2830.034)	1.040 (0.510)	0.0022 (0.002)
Test 2 Mean (SD)	1.045 (0.021)	1.061 (0.021)	7385.913 (2266.511)	0.671 (0.249)	0.00144 (0.001)
Combined Mean (SD)	**1.026 (0.021)**	**1.043 (0.019)**	**7081.432 (2507.71)**	**0.948 (0.483)**	**0.00184 (0.002)**

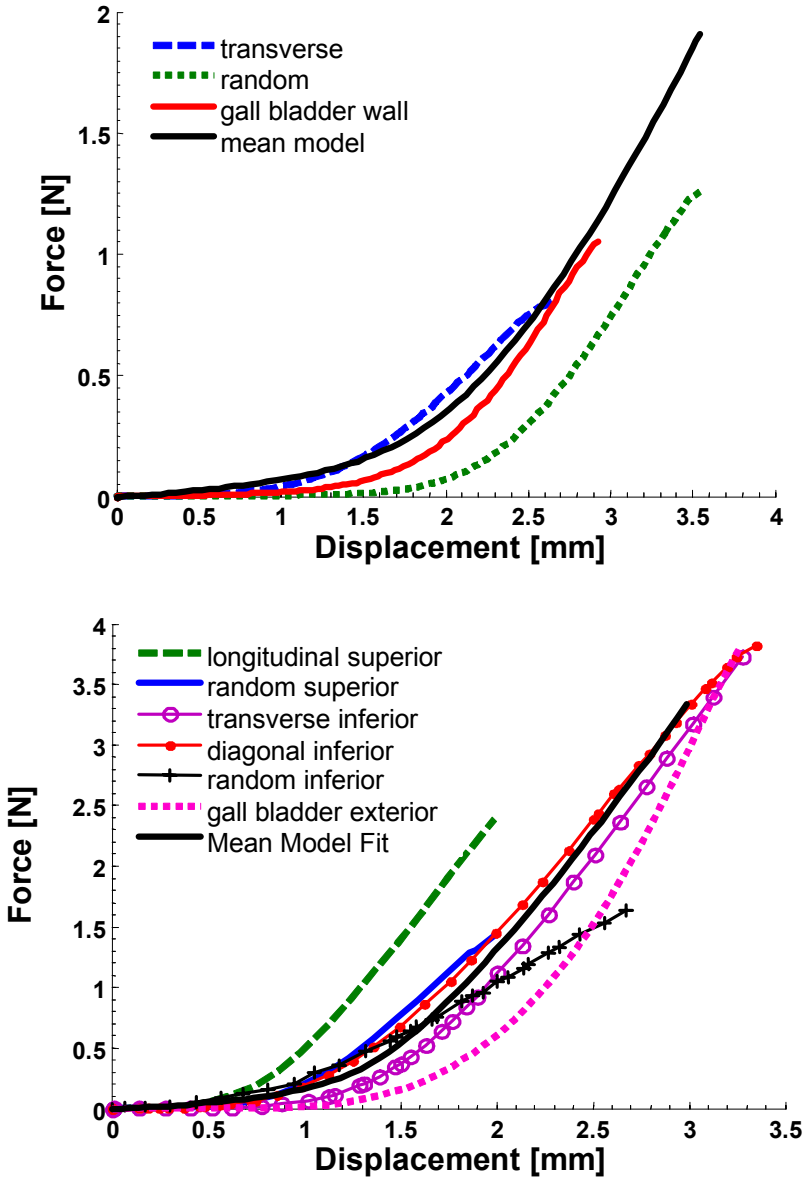

Figure 4.11 Results of uniaxial capsule model with mean parameter values and the test data.

4.5.2 Liver Ramp Indentation Optimization

Since each parameter of the constitutive relation is sensitive to the type of loading condition the tissue experiences, several deformation modalities were looked at concurrently to identity appropriate values for the parameters.

The data from the multiple ramp indentation and stress relaxation tests described in Chapter 3 were used to identify the seven parameters of the constitutive model for liver defined in section 4.3. Initially, the results of the second indentation for each speed from the first block of indentations (rate order: 2, 0.2, 20, 40 mm/s) were used to gain an

understanding of the effect each parameter had on the model's response. The results of the parameters were then used and compared to the stress relaxation data. Fitting parameters to both of these modalities in parallel provided confidence in the start values used for an optimization of a full block of multiple ramp indentation tests. It was assumed that the complete time history of 9-12 ramp indentations with a 120 second dwell time at rates spanning at least 2 orders of magnitude would capture the contribution from each parameter. However, since these models were computationally expensive to run (>20 minutes per trial), the start values obtained from looking at the stress relaxation and individual indentations at each speed was necessary.

The estimated start values and allowable ranges for the parameters outlined in section 4.3 were used to manually obtain good fits to the stress relaxation and individual indentation data at 0.2, 2, and 20 mm/s for the first liver. Start values were selected from these studies, and an optimization trial was run to identify 6 of the parameters (*m* was set to 2 from manual matching to the stress relaxation data). The force versus displacement response for each indentation was compared to the model's response after 448 iterations (Figure 4.12). The total error was based on the fit of all three curves to the data. The evolution of the parameters and the error are shown in Figure 4.13. The resulting parameters were run on a stress relaxation model and the results compared to the data (Figure 4.12). Due to the poor fit, an optimization trial was then run on the stress relaxation data using the final parameters obtained for the indentation test as start values. This was carried out for 337 iterations, and included *m*. Results for this test and the evolution of the error are shown in Figure 4.14. With better confidence in the start values and with *m* set to 2.5, a final optimization was run to identify the remaining 6 parameters using the entire set of 9 indentations and the 120 sec dwell period for the first block of the first liver comparing the force versus time data. These models took ~20 minutes to complete per trial. Final parameters were obtained after 64 iterations (Table 4.2). The resulting force versus time plots for the block of multiple indentations across speed for the model and the data, as well as the error evolution, are shown in Figure 4.15.

Table 4.2 Final optimized parameter values for liver 1. MSE is the mean squared error between the model response and the data force versus time curves for all 9 indentations and the 120-second dwell time. Units for moduli in Pa, κ_0 is in m^4/Ns.

K_s	G_p	m	S_p	μ_0	λ_L	κ_0	MSE
25,048	116.04	2.5	13,038	26.06	1.039	6.4	0.1675

The results show that the model is able to capture many of the salient features of the time-history data, including an increased peak force from the first indentation, increased peak force with loading rate, decreasing peak force with multiple indentations, nearly strain-rate independent hysteresis, and the 120 second dwell time.

Despite being able to capture many of the characteristics of the liver's response, the model fails to completely predict the observed behavior. There is clearly an underestimated hysteretic response, and an over exaggerated nonlinear curvature. The predicted rapid increase in loading force during stress relaxation also disagrees with the

data. However, realizing that absolute parameter values will take some time to achieve (discussed below), these values are used as estimates for the initial guesses of the other liver's material parameters.

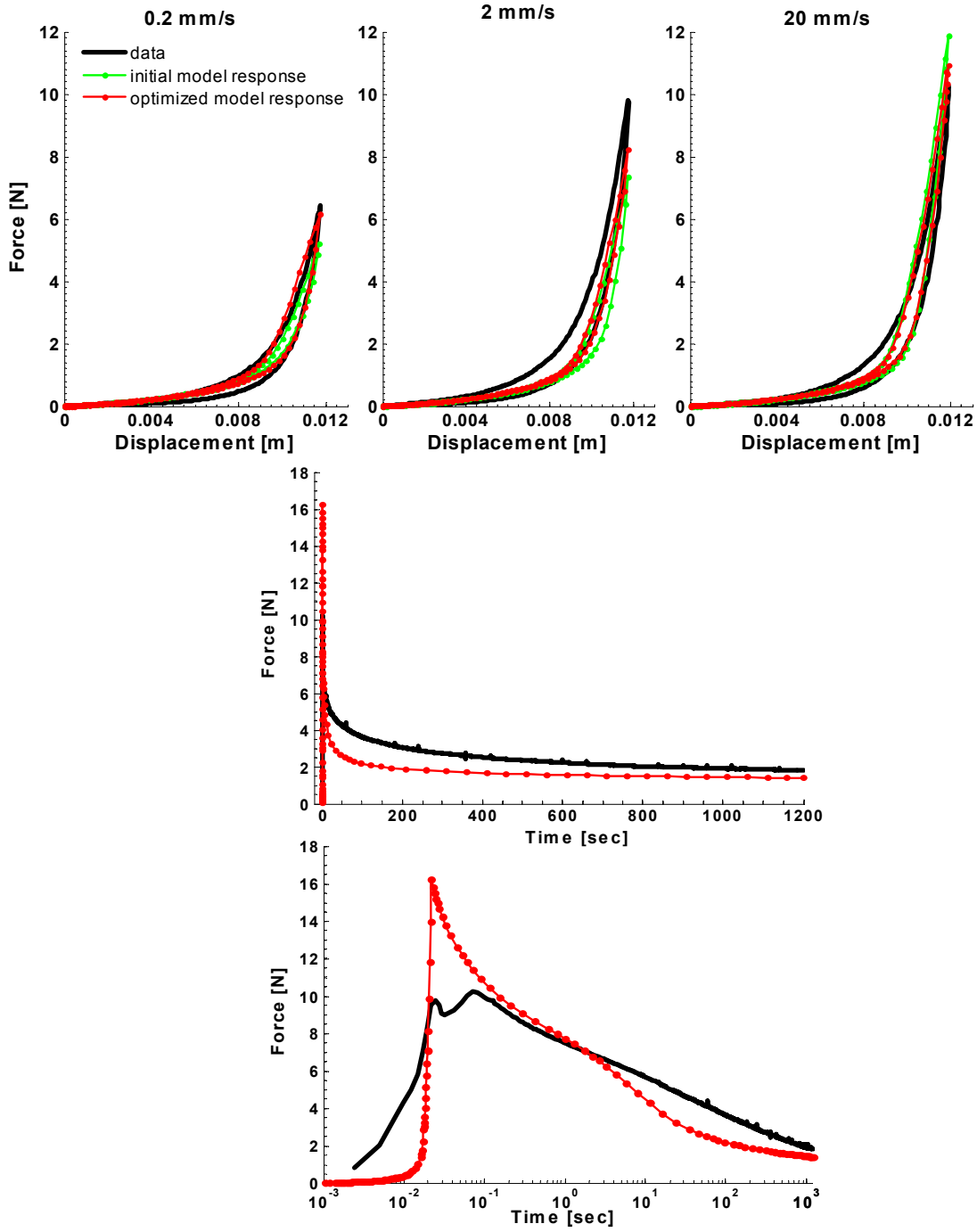

Figure 4.12 (Top) Results showing the model response (initial and final runs of the optimization) to the individual indentation data at three rates for Liver 1. (Bottom) The response using the resulting parameters compared to stress relaxation of the same liver shown in linear and log time.

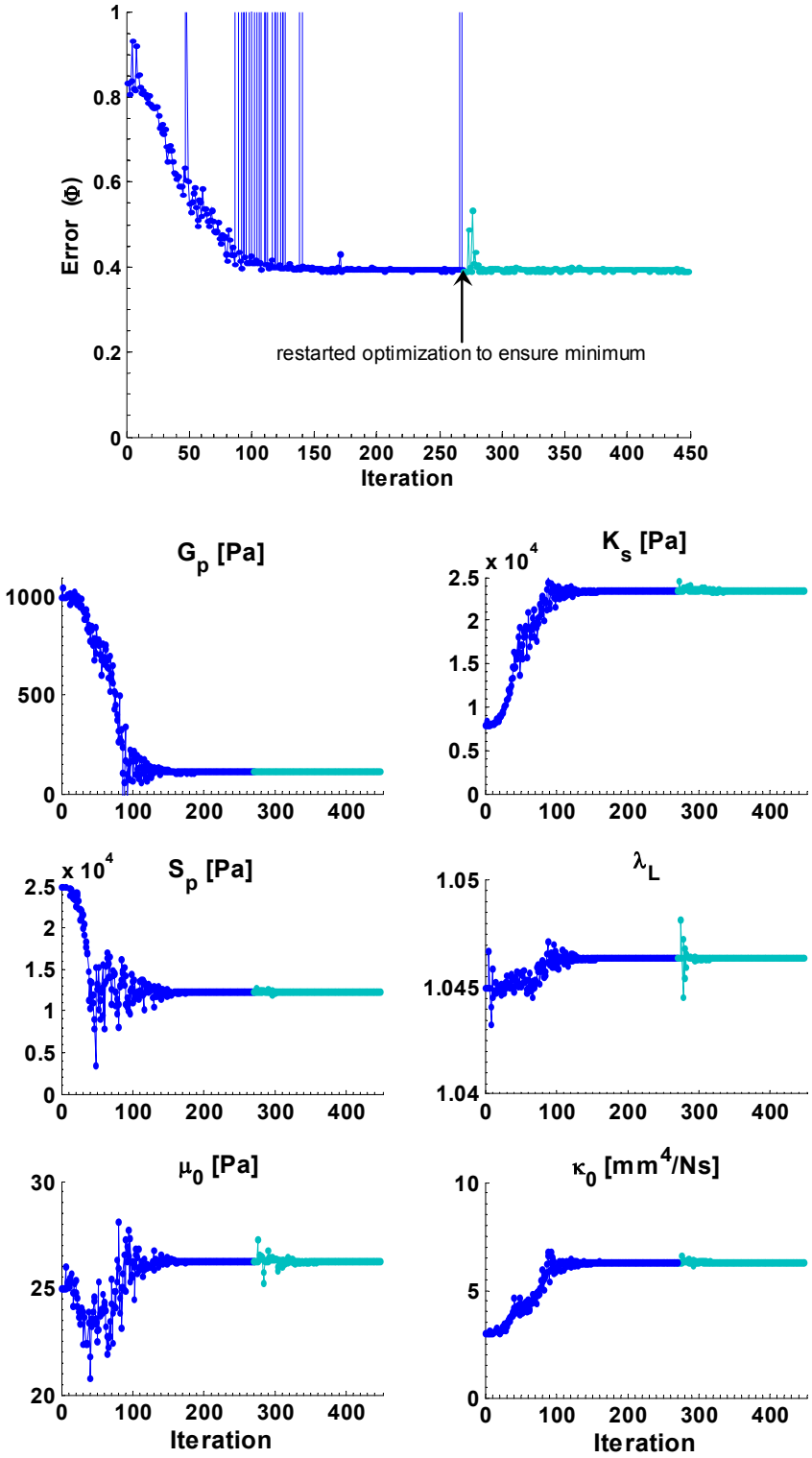

Figure 4.13 The evolution of the error and the parameter search for the 448 iterations comparing the model response to the force-displacement data of individual indentations at 0.2, 2, 20 mm/s for Liver 1 (evolution of Figure 4.12).

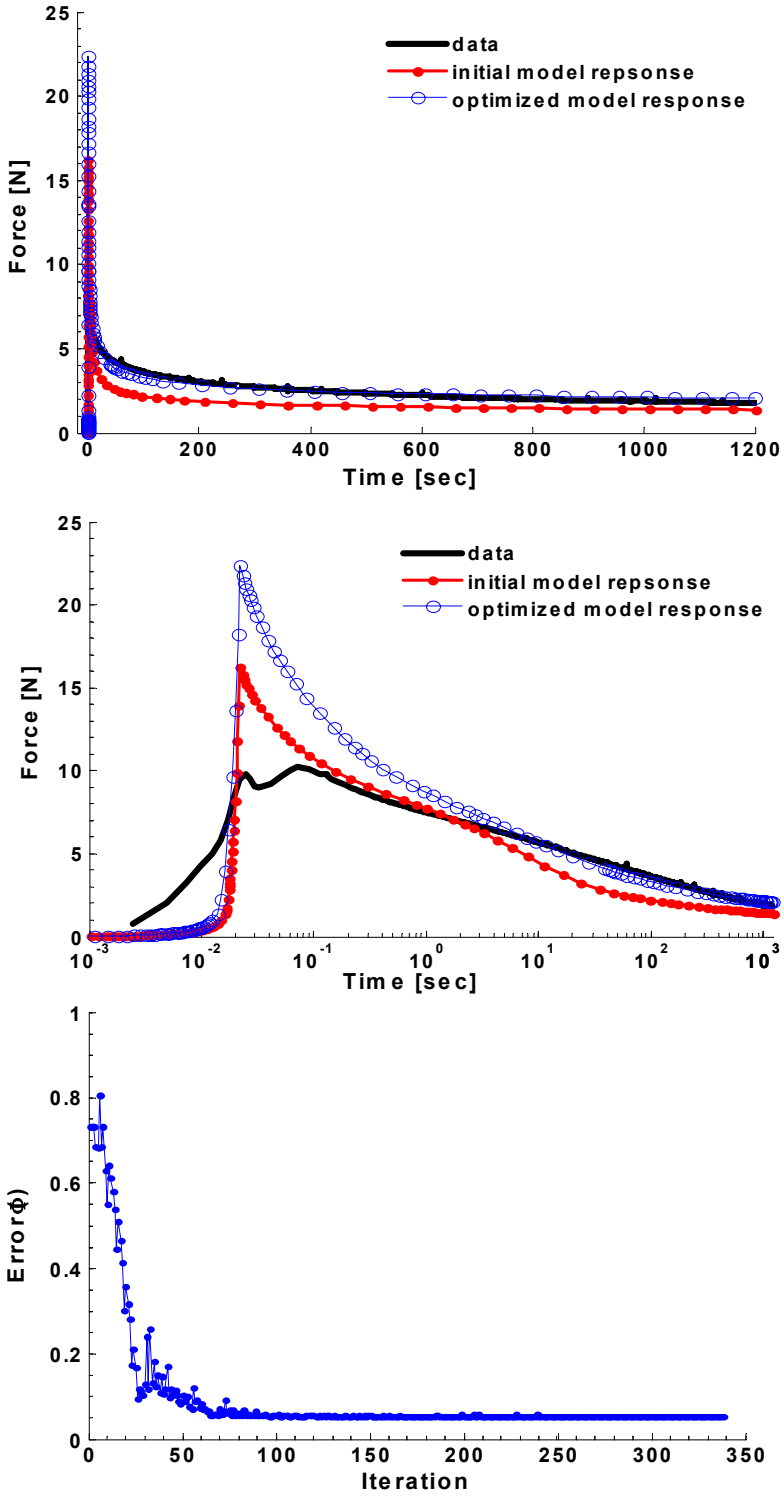

Figure 4.14 (Top) The initial and final optimized model responses compared to the data for the first stress relaxation test in Liver 1 in both. (Bottom) The evolution of the error.

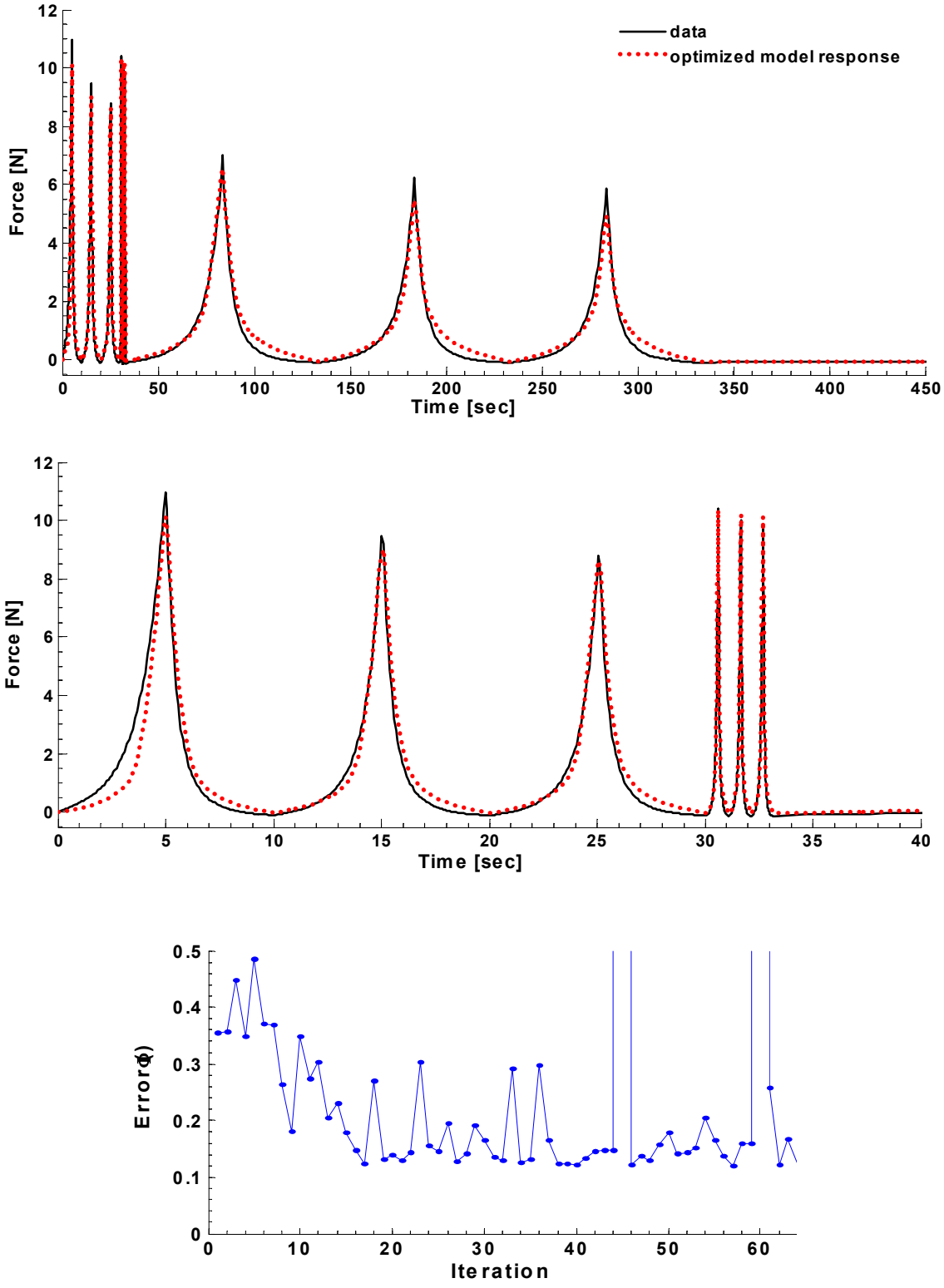

Figure 4.15 (Top) The optimized model response to the entire block of 9 indentations for Liver 1 as force versus time. (Bottom) The evolution of the error.

The third liver was modeled next, as the second had some inconsistencies in the data that the model might not be able to capture. The data from the second indentation of each speed for the first block of 12 indentations was brought through the same process described above. The first block was chosen so the first three speeds were done in the same order as the first liver modeled (2, 20, 0.2, and 40 mm/s). Using the values for the parameters in Table 4.2 as a guide, the model parameter values were manually adjusted on the 20 mm/s indentation and the stress relaxation data, until a decent match was obtained (Figure 4.16). The optimization across 4 speeds and all 7 parameters was run for 134 iterations. Although the MSE was slowly improving, the results were converging poorly. Therefore, the values for the parameters at run 134 were used to fully optimize the stress relaxation response instead. The results of this optimization (483 iterations) are shown in Figure 4.17. The single indentation at 4 speeds was run again with the newly identified parameters as the start values and *m* set to the stress relaxation optimized value of 1.18. This search was stopped after 158 iterations as the results were again converging poorly. The force versus displacement data for the 4 indentations is shown in Figure 4.18 along with the "optimized" responses for each of the trials run. The resulting values for the parameters from the stress relaxation, and both indentation optimizations are shown in Table 4.3.

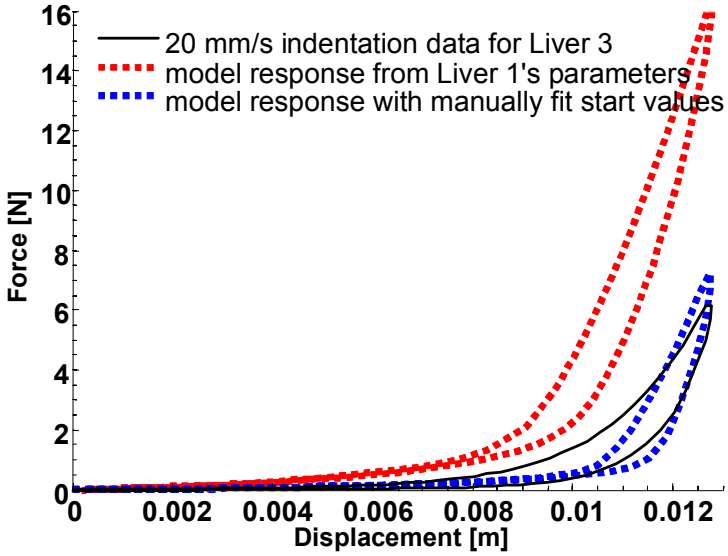

Figure 4.16 The model's response to the first block of the 3rd liver's second 20 mm/s indentation. The red dotted line used the parameters identified for Liver 1. The blue dotted line is a manual fit used to obtain start values for the optimization.

Due to the poor agreement in parameter values seen in Table 4.3, an optimization for the entire block was not attempted. However, a model of the full block was run using the mean values of the parameters, and the results are shown in Figure 4.19. Although clearly not an exact fit, the model is capable again of capturing the salient features of the data with the exception of the 40 mm/s peak forces. Similar issues as were described for the first liver are observed. Namely, the model fails to capture the true hysteresis, and is

unable to obtain an appropriate loading response for all speeds. In particular, the 40 mm/s indentations not only had peak forces

Table 4.3 Constitutive law parameter values for Liver 3 from three different optimization trials. Units for moduli in Pa, κ_0 is in m^4/Ns.

TEST	K_s	G_p	m	S_p	μ_0	λ_L	κ_0	MSE
Indentation Trial 1	8,253	40.8	1.495	4,447	8.579	1.051	9.774	0.674
Stress Relaxation	14,914	69.3	1.187	3,142	1.404	1.040	0.860	0.023
Indentation Trial 2	15,569	43.7	*1.18 (set)*	2,393	1.354	1.054	1.022	1.39
Mean	12,912	51.3	1.287	3,327	3.780	1.048	3.885	-

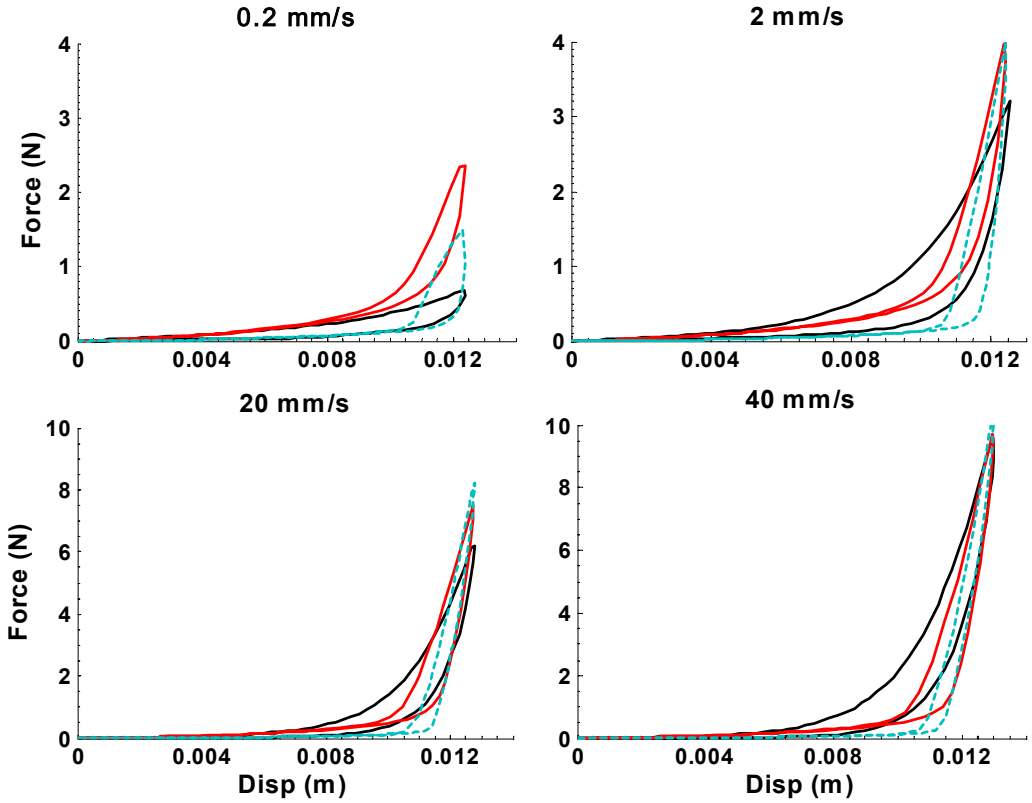

Figure 4.18 Model responses for two different optimization trials compared to the second indentation of each speed for liver 3. Black is the data, red is the 134th trial of the optimization of all 7 parameters from the manually fir start estimate in Figure 4.17 (MSE = 0.6742), and blue dashed is the 158th trial of an optimization with the parameter results from the stress relaxation test as start values (MSE=1.39).

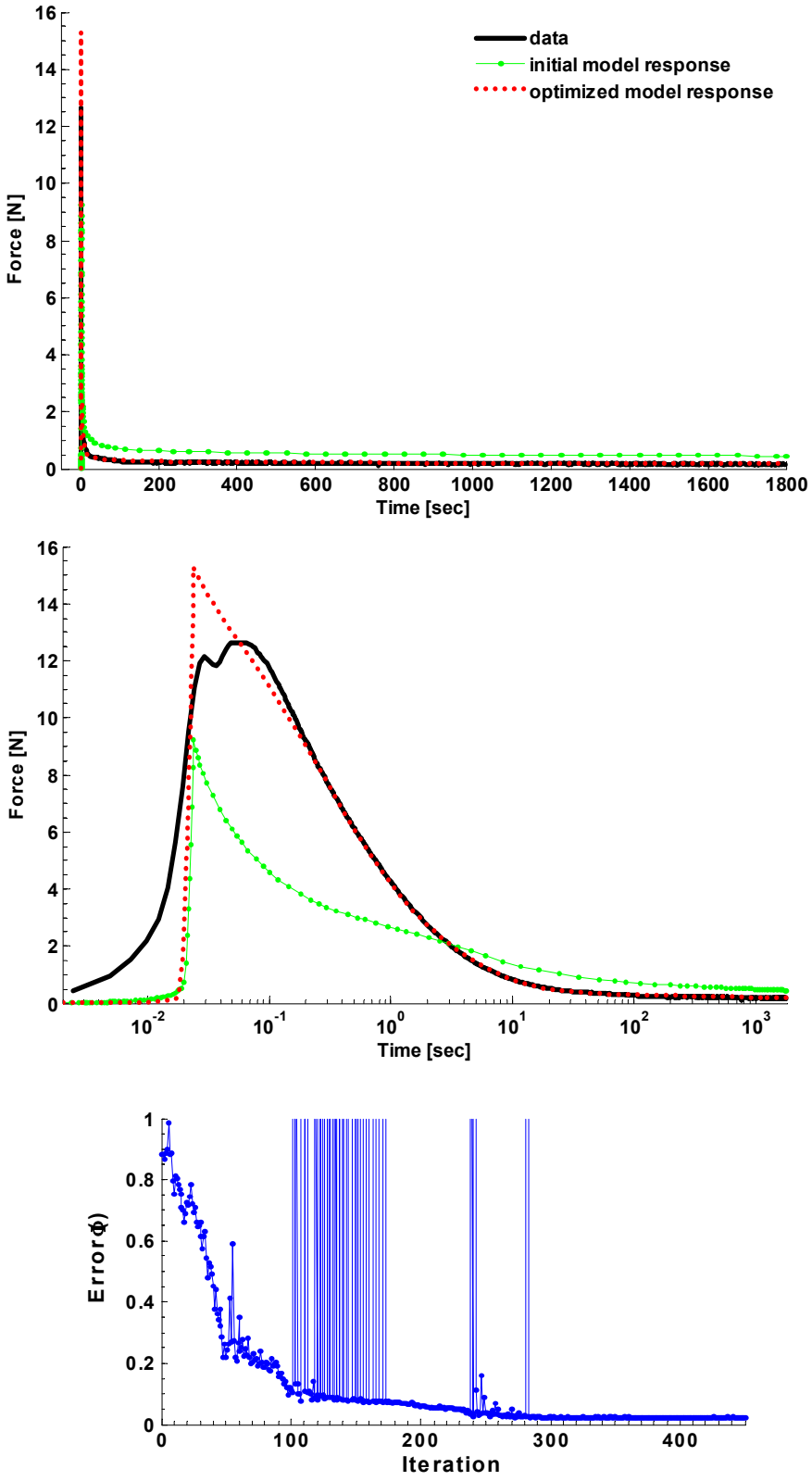

Figure 4.17 (Top) The model response to stress relaxation for liver 3 compared to the data with both initial and optimized parameters shown in both linear and log time. (Bottom) The evolution of the error function.

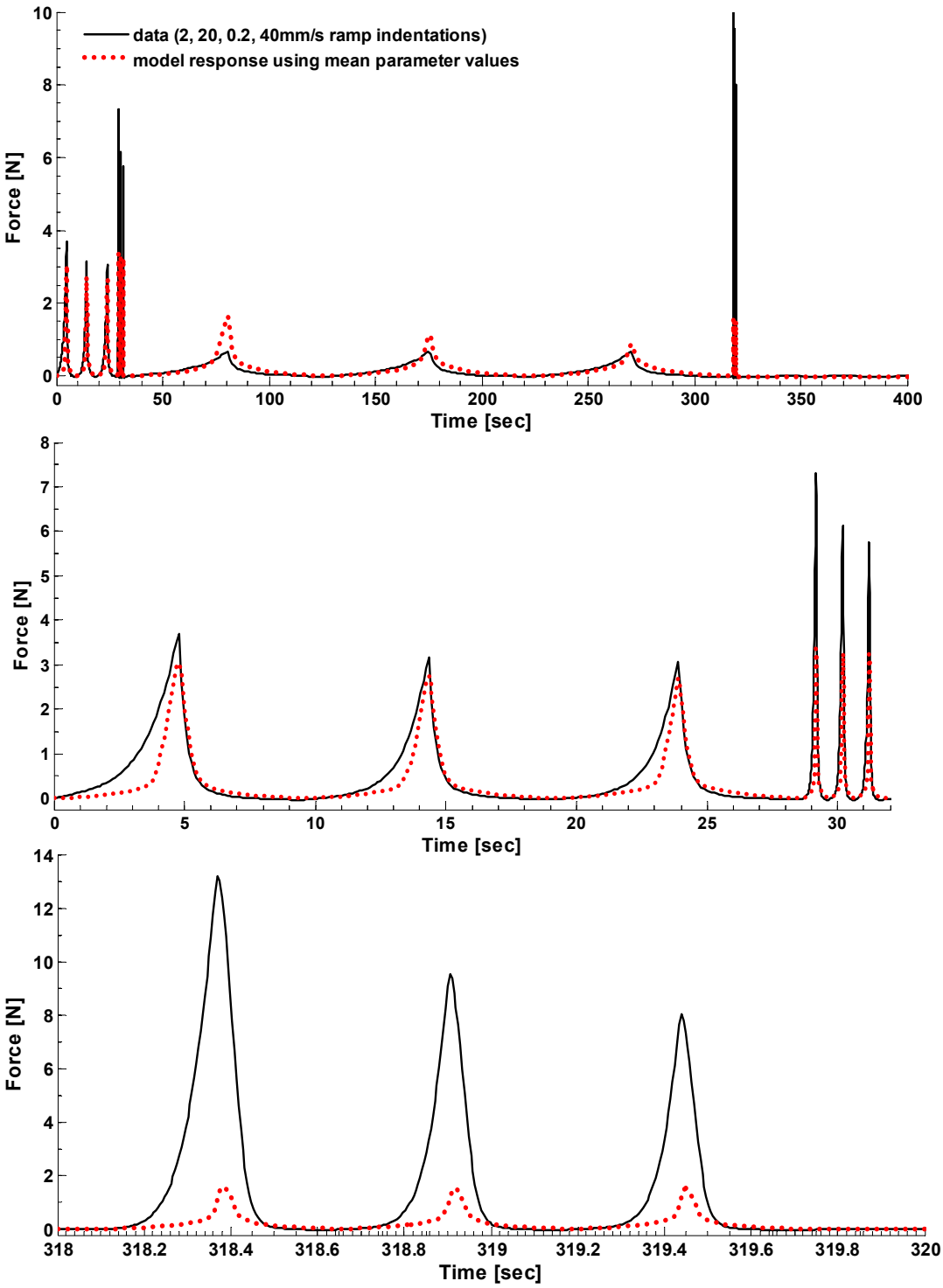

Figure 4.19 Force versus time data from the first block of data for liver 3 and the model response using the mean material parameters in Table 4.3.

Similar issues as were described for the first liver are observed. Namely, the model fails to capture the true hysteresis, and is unable to obtain an appropriate loading

response for all speeds. In particular, the 40 mm/s indentations not only had peak forces that were 20% of what they should be, but also were smaller than the forces for the 2 and 20 mm/s indentations. This suggests that perhaps not enough fluid returned to the indented volume indicating that the permeability was too low.

4.5.3 Validation

Although it was already shown that the results of one liver might not necessarily be true for another liver, testing the predictive capability of the model can still validate the identified parameter ranges. This was done by using the final values of the parameters in Tables 4.2 and 4.3 and modeling the response to the creep response. Figure 4.20 shows the results of this validation using the data from the first liver (recall that all creep data were similar in Chapter 3). The material parameters for the first liver capture the initial dynamic behavior, but do not bode well over time. The mean material parameters identified for the third liver actually produce a better fit to the data, particularly in the steady-state case. This suggests that the elastic moduli are too stiff for the first liver, since they are half the magnitude of those in the third liver, and that the viscous parameters for the third liver are better matched to the liver's actual response: having a softer shear stretch and lower exponent for the parenchyma network.

Although not uniquely identified, the results of the various optimization trials suggest a working range for each parameter. These are presented in Table 4.4.

Table 4.4 Range of material parameter values during the optimization of the first and third livers.

	K_s [Pa]	G_p [Pa]	m	S_p [Pa]	μ_0 [Pa]	λ_L	κ_0 [m^4/Ns]
Parameter Range During Optimization (Max – Min)	6,615 - 25,048	40.3 - 116.0	1.18 - 2.50	2,393 - 14,214	1.35 - 28.96	1.035 - 1.051	0.86 - 11.2

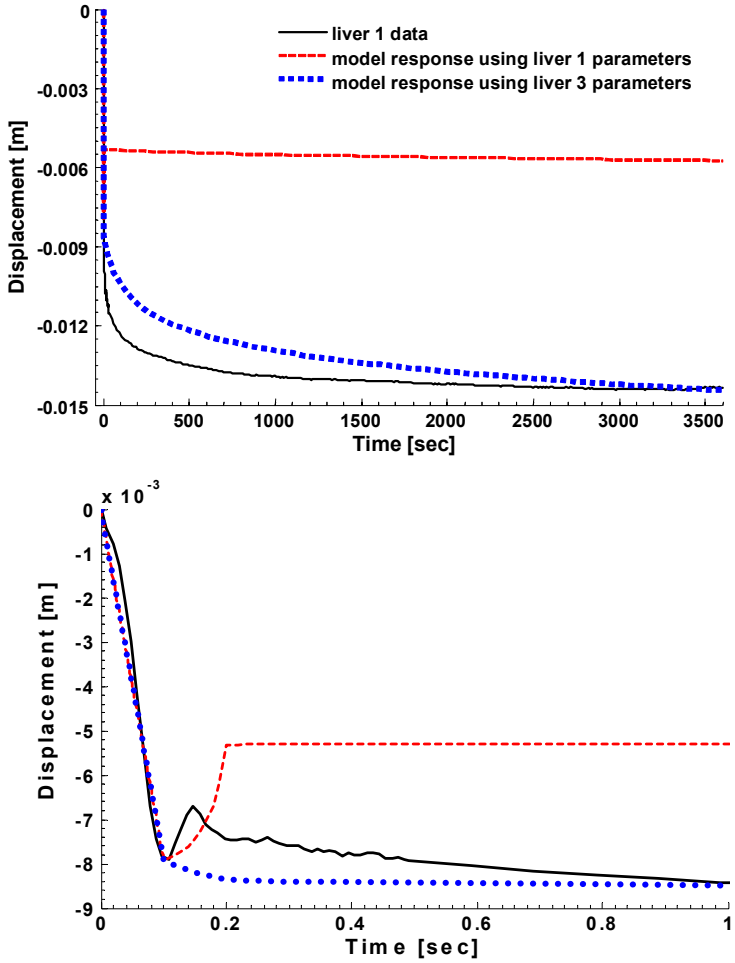

Figure 4.20 Model prediction of the creep response of liver 1 using the parameter identified for liver 1 in Table 4.2, and the parameters found for liver 3 in Table 4.3.

4.6 Discussion

This chapter presents the development of a physically-based nonlinear constitutive model for liver, under finite deformations typical of surgical manipulation. Although others have tried to model the mechanical response of liver (Brown, et al. 2003; Carter, et al. 2001; Chen, et al. 1996; Hu and Desai 2003; Kim, et al. 2003; Liu, et al. 2004; Liu and Bilston 2000; Miller 2000b; Ottensmeyer 2001; Picinbono, et al. 2001), no one has captured the finite deformation, viscoelastic response of liver with a physically-based model like the one described here. Most models assume some form of linearity, incompressibility, and are incapable of handling large strain indentation over time. The closet model is one presented by Snedeker et al for the kidney (2005a). They model the impact failure of the entire kidney using a multi-constitutive model approach. The model represents the capsule, parenchyma, calyses, renal pelvis, and fluid within the kidney. The capsule is modeled with a nonlinear Cowper-Symonds model (Snedeker, et al. 2005b). The response of the parenchyma is modeled using a second order Mooney-Rivlin strain energy function with second order prony viscosity. The calyses and renal pelvis are considered to be

linear elastic fluid filled tubes and the blood vessels are treated as pressurized tubes filled with a linear elastic fluid (represented with a low shear modulus). Despite obtaining good agreement to their impact data, it is unlikely that a model for the kidney under such conditions could represent the liver under surgically relevant deformation.

This chapter described a model and a technique towards realizing the material parameters of the liver's components. The constitutive framework developed shows promise is representing solid perfused organs like the liver, under finite deformations. Shortcomings of the model's ability to predict the true viscoelastic response of the results obtained in Chapter 3, suggest that some improvements to the model ought to be considered.

One of the strengths of this model is the recognition that soft biological tissues are compressible. Although the total stress can be separated into components from its isochoric (deviatoric) and volumetric (hydrostatic) responses, assuming that the changes in volume come solely from the fluid response is an over simplification. In reality, the overall change in volume should come from an initial change in volume from the fluid moving out (the permeability network) and from the collagen network losing water over time. Allowing the collagen to contribute to the volumetric response would result in an additional material parameter: a prestretch λ_0. Having a pre-stretch is relevant since the fibrous component of biological materials are in a state of pretension to balance the osmotic pressure depending on the level of hydration of the tissue. This prestretch gives rise to a residual stress observed in other tissues, which is considered necessary for successful modeling of finite deformation behavior (Bischoff, et al. 2000). The curvature of the force displacement response will likely improve (soften) by adding a prestretch to the model, and by allowing the collagen to change volume, albeit slightly. Jordan et al presented the effects of this prestretch in a breast pathology model (Jordan, et al. 2005a).

Other potential changes to the model include adding a relaxation term to the capsule. The creep response from the model proved to be much stiffer than that of the data. Relaxing the parameters of the capsule helped achieve a more desirable response. The results of the uniaxial tension tests to failure were likely not enough information to establish an appropriate model for the capsule. Stress relaxation and/or creep tests on the capsule should be carried out to understand the time dependencies of the tissue (Prevost 2006). The creep indentation test also assumed a frictionless contact condition. Dedicated tests in the future should use the motorized suction indenter to ensure known boundary conditions.

The axisymmetric assumption inadvertently forces the fluid to stay contained within the confines of the given mesh geometry. The fluid has nowhere to dissipate to during long time-constant tests, such as the hour long creep tests. The model therefore predicts higher steady-state forces than what is observed. Future models should reconsider the geometric assumptions, and better model the flow path of the vasculature.

Lastly, while the optimization results produced believable fits between the model and experimental data, the issues of global convergence and uniqueness of solution need to be addressed. The results presented here suggest that solving the inverse problem of a 7-dimensional solution space is not straightforward, and that the initial estimates for the parameter values is critical in ensuring that convergence is met. There are at least two ways in which to address this critical dependence on the initial parameter values. A densely sampled, exhaustive search of the 7-dimensional parameter space, could be used

to understand the contour of the solution space. Although extremely helpful in providing an overall understanding of the parameter space, and in addressing the issue of uniqueness, the large computational expense for performing such a search is daunting. Another approach would be to solve the model analytically by simplifying the results of the indentation tests with a uniaxial compression approximation. A linear attempt is presented in Appendix B.

The technique presented in this chapter also suggests that optimizing different modes of time-dependant deformation simultaneously may be better than doing them sequentially. To keep the computational cost of this initial search to a minimum, it is suggested that a single indentation from each speed of the multiple ramp tests and one from the stress relaxation tests be optimized together for all independent material parameters. The error function may also need to be revised. Other measures for error were tried in an attempt to match peak force, hysteresis, initial slope, and curvature. These measures failed to improve the outcome. However, other measures of error should be considered that perhaps weigh the short and long term response of the stress relaxation more equally, etc.

In conclusion, this chapter describes a physically based, physiologically relevant, nonlinear 3D constitutive relation for the liver. The goal of this thesis work was to create a "ground-truth" physically relevant model for liver. Simplifications to the model will be required for implementation into surgical simulations that require large deformations to run in real-time. The next chapter addresses how to evaluate such simplifications by assessing the speed versus accuracy tradeoff that exists in real-time soft tissue modeling.

Appendix B

Linear Analytical Approximation of the Constitutive Model

In this appendix, the constitutive model presented in Chapter 4 is simplified to an analytical linear approximation. This representation can be used to ensure that the form of the constitutive model is correct, and to determine approximate start values for the material parameters. A nonlinear analytical representation could obtain values for the model's actual material parameters.

The indentation data is represented with a uniaxial compression approximation. The volume of tissue under the indenter is assumed to be the same as a uniaxial section with dimensions equal to 1.5 times the radius of the indenter (R), and with the same thickness (h) (Figure A2.1). With this approximation, stresses and strains can be used instead of forces and displacements, and both sides of the model can be assumed to experience the same strain.

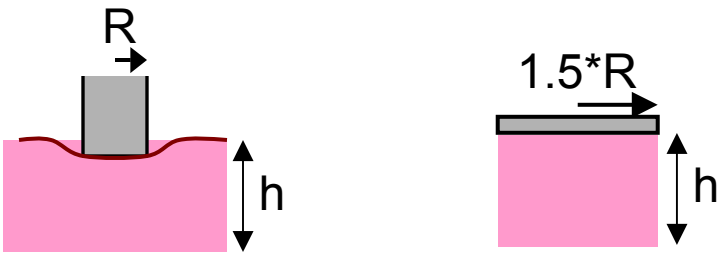

Figure A2.1 Representing the indentation scenario (Left) with a uniaxial approximation (Right).

The lumped parameter model is therefore simplified into the isochoric and volumetric parts with linear springs and dashpots replacing the nonlinear and biphasic components (Figure A2.2). The isochoric side can be treated as a standard linear solid viscoelastic model with a shear modulus G, and the volumetric side is a simple Voigt viscoelastic model with bulk modulus B.

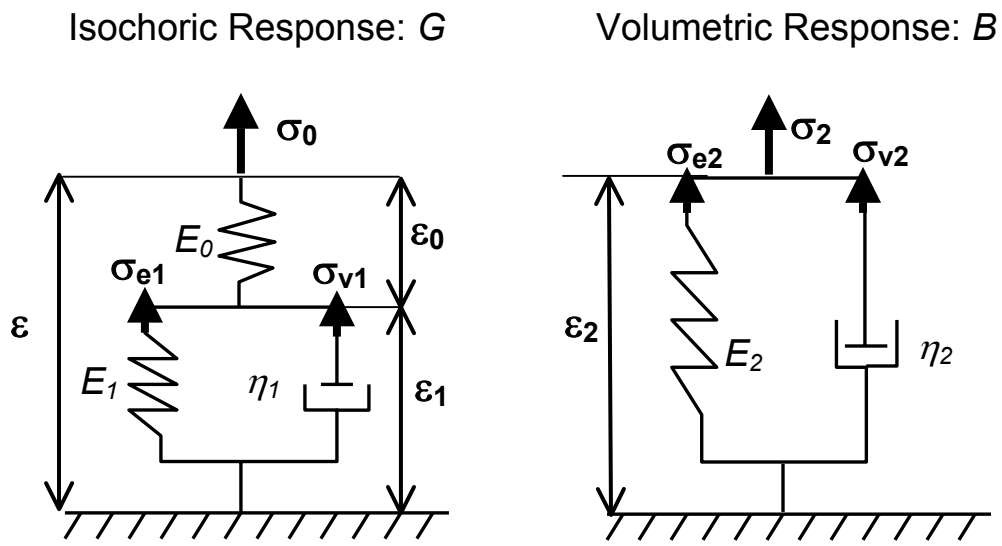

Figure A2.2 Schematic representation of the simplified tissue model.

$$\sigma_0 = \boldsymbol{E}_0\varepsilon_0 = \sigma_1 = \sigma_{e1} + \sigma_{v1} \quad \text{A2.1}$$

$$\sigma_{e1} = \boldsymbol{E}_1\varepsilon_1 \quad \text{A2.2}$$

$$\sigma_{v1} = \eta_1\dot{\varepsilon}_1 \quad \text{A2.3}$$

$$\varepsilon = \varepsilon_0 + \varepsilon_1 \quad \text{A2.4}$$

$$\sigma_2 = \sigma_{e2} + \sigma_{v2} \quad \text{A2.5}$$

$$\sigma_2 = \boldsymbol{E}_2\varepsilon_2 + \eta_2\dot{\varepsilon}_2 \quad \text{A2.6}$$

$$\varepsilon = \varepsilon_2 \quad \text{A2.7}$$

The ramp displacement waveform is approximated by a step displacement plus a sinusoidal waveform for ease of analysis. Therefore, assuming that both sides of the model experience the same strain (Equation A2.7), the strain and strain rate can be represented by

$$\varepsilon(\boldsymbol{t}) = \varepsilon - \varepsilon_i \sin\ \omega\boldsymbol{t} \quad \text{A2.8}$$

$$\dot{\varepsilon}(\boldsymbol{t}) = -\varepsilon_i\omega\cos\omega\boldsymbol{t} \quad \text{A2.9}$$

where ε_i is the initial strain, ω is the frequency of the sine wave and t is time. The stress response for the sine wave part is assumed to also be a sine wave shifted in time by phase shift δ,

$$\sigma(\boldsymbol{t}) = -\sigma_i \sin(\omega\boldsymbol{t} + \delta) \quad \text{A2.10}$$

$$\dot{\sigma}(\boldsymbol{t}) = -\sigma_i\omega\cos(\omega\boldsymbol{t} + \delta) \quad \text{A2.11}$$

while the step response is assumed to have an exponentially decaying stress response. Substituting equations A2.8-11 into equations A2.1-6 results in the equation of motion for each side

$$\sigma_0(t) = \varepsilon_i \left(\frac{E_0 E_1}{E_0 + E_1} \right) \left[1 - e^{-t\left(\frac{E_0 + E_1}{\eta_1} \right)} \right] + \left(\frac{E_0 \varepsilon_i}{(E_0 + E_1)^2 + \omega^2 \eta_1^2} \right) \left[\sin \omega t \left(E_1 (E_0 + E_1) + \omega^2 \eta_1^2 \right) + \cos \omega t (E_0 \eta_1 \omega) \right] \quad \text{A2.12}$$

$$\sigma_2(t) = -E_2 \varepsilon_i - \varepsilon_i \left[\sin \omega t (E_2) + \cos \omega t (\eta_2 \omega) \right] \quad \text{A2.13}$$

The right hand term of each equation of motion is the response from the sinusoidal input, and these can be used to determine the shear and bulk storage (in phase) and loss (out of phase) moduli (G_S, G_D, B_S, B_D) and the shear and bulk complex moduli (G^*, B^*)

$$G_S = \frac{E_0 \left(E_1 (E_0 + E_1) + \omega^2 \eta_1^2 \right)}{(E_0 + E_1)^2 + \omega^2 \eta_1^2} \quad \text{A2.14}$$

$$G_D = \frac{\omega \eta_1 E_0^2}{(E_0 + E_1)^2 + \omega^2 \eta_1^2} \quad \text{A2.15}$$

$$G^* = (G_S + i G_D) \quad \text{A2.16}$$

$$B_S = E_2 \quad \text{A2.17}$$

$$B_D = \omega \eta_1 \quad \text{A2.18}$$

$$B^* = (B_S + i B_D) \quad \text{A2.19}$$

Assuming uniaxial compression, an overall elastic moduli (E^*) for the model can be represented by

$$E^* = \frac{9 B^* G^*}{G^* + 3 B^*} = E_S + i E_D \quad \text{A2.20}$$

where the storage (E_S) and loss (E_D) moduli for the whole model can be determined by substituting equations A2.14-A2.19 into A2.20.

$$E_S = \frac{9 E_0 (num)}{den} \quad \text{A2.21}$$

$$num = \left(3 \left(E_1^2 + \omega^2 \eta_1^2 \right) \left(E_2^2 + \omega^2 \eta_2^2 \right) + E_0 \left(E_2 \left(E_1^2 + 3 E_1 E_2 + \omega^2 \eta_1^2 \right) + 3 \omega^2 E_1 \eta_2^2 \right) \right) \quad \text{A2.22}$$

A2.23

$$\boldsymbol{den} =$$
$$9\left(\boldsymbol{E}_1^2+\omega^2\eta_1^2\right)\left(\boldsymbol{E}_2^2+\omega^2\eta_2^2\right)+6\boldsymbol{E}_0\left(\boldsymbol{E}_2\left(\boldsymbol{E}_1^2+3\boldsymbol{E}_1\boldsymbol{E}_2+\omega^2\eta_1^2\right)+3\omega^2\boldsymbol{E}_1\eta_2^2\right)+\boldsymbol{E}_0^2\left(\left(\boldsymbol{E}_1+3\boldsymbol{E}_2\right)^2+\omega^2\left(\eta_1+3\eta_2\right)^2\right)$$

$$\boldsymbol{E_D}=\frac{9\omega\boldsymbol{E}_0^2\left(3\boldsymbol{E}_2^2\eta_1+\eta_2\left(\boldsymbol{E}_1^2+\omega^2\eta_1\left(\eta_1+3\eta_2\right)\right)\right)}{\boldsymbol{den}} \qquad \text{A2.24}$$

At high and low frequencies the loss modulus tends towards zero while the storage modulus reduces to

$$\lim_{\omega\to\infty}\left(E_S\right)\to 3E_0 \qquad \text{A2.25}$$

$$\lim_{\omega\to 0}\left(E_S\right)\to\frac{9E_0E_1E_2}{3E_1E_2+E_0\left(E_1+3E_2\right)} \qquad \text{A2.26}$$

The tangent of the phase shift is taken to be the loss modulus divided by the storage modulus

$$\tan\delta=\frac{\omega\boldsymbol{E}_0\left(3\boldsymbol{E}_2^2\eta_1+\eta_2\left(\boldsymbol{E}_1^2+\omega^2\eta_1\left(\eta_1+3\eta_2\right)\right)\right)}{3\left(\boldsymbol{E}_1^2+\omega^2\eta_1^2\right)\left(\boldsymbol{E}_2^2+\omega^2\eta_2^2\right)+\boldsymbol{E}_0\left(\boldsymbol{E}_2\left(\boldsymbol{E}_1^2+3\boldsymbol{E}_1\boldsymbol{E}_2+\omega^2\eta_1^2\right)+3\omega^2\boldsymbol{E}_1\eta_2^2\right)} \qquad \text{A2.27}$$

Assigning values for the spring and dashpot constants, the storage modulus, loss modulus, and tanδ (Equations A2.21, A2.24, A.27) are plotted versus frequency in Figure A2.3. The values for the constants are: E_0 = 5,131.4 Pa (from a spring constant K_0 = 50 N/m), E_1= 513.15 Pa (from a spring constant K_1 = 5 N/m), E_2= 2,565.7 Pa (from a spring constant K_2 = 25 N/m), η_1= 10,263 Pa s (from a dashpot constant b_1 = 100 Ns/m), and η_2= 1,026.3 Pa s (from a dashpot constant b_1 = 10 Ns/m).

Given Figure A2.3 and the equations presented above, the constants for the model can be determined. A more robust interpretation of the model would provide a better estimation of the model parameters by comparing the predicted moduli to the moduli from the single ramp rate data collected in Chapter 3. Changes to this analytical model would include using the appropriate nonlinear springs and dashpots and using the combined modulus for indentation in place of Equation A2.20 (although meant for infinitesimal strains)

$$E^*=\frac{12G^*\left(-3B^*+G^*\right)^2}{\left(9B^*-4G^*\right)\left(3B^*+G^*\right)} \qquad \text{A2.28}$$

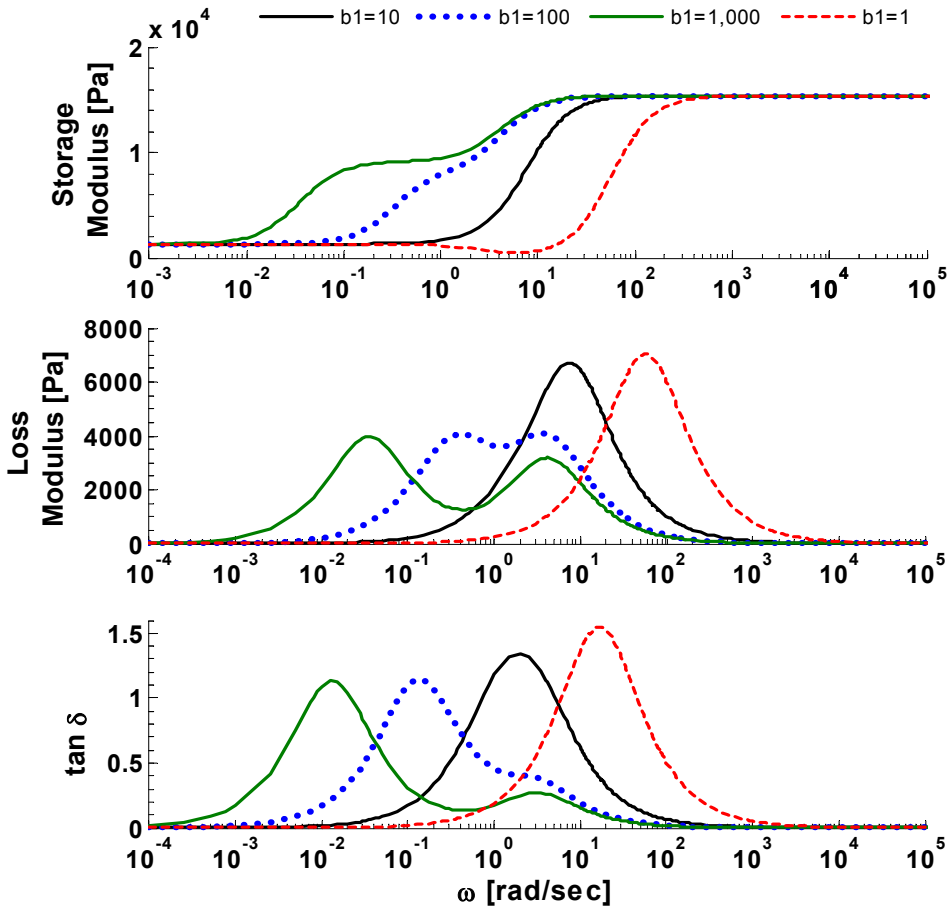

Figure A2.3 The storage modulus (Top), loss modulus (Middle), and tanδ (Bottom) of the linear model across frequency. The different curves represent different values for the isochoric dashpot [units for b= Ns/m].

Appendix B Jordan & Howe Poster

Mechanical Characterization of Soft Tissues with Three-Dimensional Ultrasound Imaging

Petr Jordan[1,2], Robert D. Howe[1,2]

[1]Division of Engineering and Applied Sciences, Harvard University, Cambridge, MA

[2] Division of Health Sciences and Technology, MIT/Harvard, Cambridge, MA

ABSTRACT

The ability to accurately model mechanical properties of soft tissues plays a fundamental role in the future advances in surgical simulation, planning, and assistance. While a physically based mathematical model capable of capturing the complex behavior of soft tissues has been formulated, the identification of unique model parameters remains a challenge. The goal of this project is to combine traditional indentation testing with three-dimensional ultrasonic imaging to capture the mechanical response of in vivo soft tissue and, with this information, uniquely identify a set of optimal model parameters. This technique is currently being developed for modeling the response of liver tissue but will be extended in the future to other soft tissues, including those of spleen, kidney, breast, and brain. The development of this technique is a key step toward image-driven tissue modeling and characterization.

METHODS

Experimental Approach

Characteristic force-displacement relationships are obtained from an indentation of porcine liver while imaging with 3D ultrasound (Philips SONOS 7500 Live 3D Echo, Philips Medical Systems, Andover, MA, USA), providing the ability to estimate the complete three-dimensional deformation field of the sample under indentation.

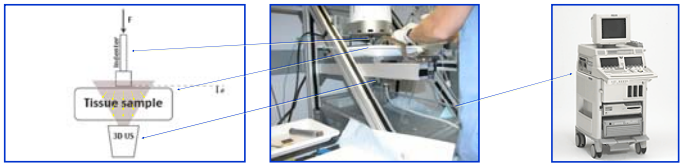

The stress-strain characteristics of biological tissues are known to be largely nonlinear, rate dependent, and dissipative. Our soft tissue model [2,3] consists of a collagen-elastin structural component in the form of an extended Arruda-Boyce hyperelastic law, a cellular interaction modeled as a nonlinear viscous solid, and an organ vascular perfusion modeled by a pressure-driven diffusion process. The response of the model is fitted to in-vitro porcine liver indentation experiments through iterative finite-element modeling.

• iterative FEM parameter estimation framework is used to match the experimental response to a mechanical organ model

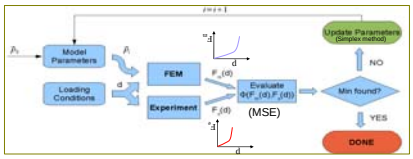

• material parameters are found by minimizing:

$$\Phi(\lambda_0,\lambda_L,\mu,k,\kappa)=\frac{1}{N}\sum_{i=1}^{N}\left(F_{model}(d_i,\lambda_0,\lambda_L,\mu,k,\kappa)-F_{experiment}(d_i)\right)^2$$

Optical Flow Formulation

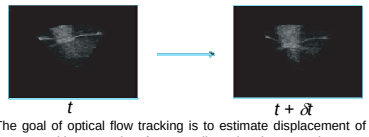

The goal of optical flow tracking is to estimate displacement of every voxel between data frames collected at times *t* and *t* + δ*t*.

• Under intensity (*E*) constancy assumption, the displacement (*u,v,w*) of a voxel from time *t* to *t*+δ*t* :

$$I(x+u\delta t,y+v\delta t,z+w\delta t,t+\delta t)=I(x,y,z,t)$$

• Resulting, upon Taylor series linearization, in the *optical flow constraint* :

$$\frac{\partial I}{\partial x}u+\frac{\partial I}{\partial y}v+\frac{\partial I}{\partial z}w-\frac{\partial I}{\partial t}=0$$

• *n* voxels results in *n* equations and 3**n* unknows and requires additional constraint

One of the limitations of indentation testing methods is the area of uniqueness and sensitivity of model parameters to experimental observations. In order to improve the tissue testing process, we present a 3D ultrasound imaging technique, which captures the experimental tissue deformation during indentation. We employ computer vision techniques to track tissue deformation with a novel optical flow algorithm. Standard optical flow algorithms are not explicitly consistent with solid organ mechanics and tend to bias their deformation estimate toward the motion of an idealized incompressible linear solid. Our work has addressed this limitation by a development of a regularization framework capable of coupling optical flow equations to fundamental soft tissue biomechanics.

Horn and Schunck Approach [4]

Find voxel displacements (u,v,w) that minimize:

$$\Psi(\alpha)=\iiint\left(\Psi_0(x,y,z,t)+\alpha^2\Psi_s(x,y,z,t)\right)dxdydz$$

(Optical flow constraint + Smoothness constraint)

$$\Psi_s=\left(\frac{\partial u}{\partial x}\right)^2+\left(\frac{\partial u}{\partial y}\right)^2+\left(\frac{\partial u}{\partial z}\right)^2+\left(\frac{\partial v}{\partial x}\right)^2+\left(\frac{\partial v}{\partial y}\right)^2+\left(\frac{\partial v}{\partial z}\right)^2+\left(\frac{\partial w}{\partial x}\right)^2+\left(\frac{\partial w}{\partial y}\right)^2+\left(\frac{\partial w}{\partial z}\right)^2$$

$$\Psi_0=(E_x u+E_y v+E_z w+E_t)^2$$

Resulting Laplacian smoothing operator:

$$\nabla^2 u=0$$

FEM-Constrained Optical Flow

Optical flow solved as a mechanical system:

Per-node least-square estimation of *(u,v,w)* and (c_x,c_y,c_z) → (Linear springs of length (u,v,w) and stiffness (c_x,c_y,c_z)) → Full displacement field from mechanical FEM model

Smoothing operator for linear elastic materials:

$$\frac{E}{(1+\nu)(1-2\nu)}\nabla(\nabla\cdot u)+\frac{E}{2(1+\nu)}\nabla^2 u=0$$

Mechanics / Optical Flow Coupling

Solving the Optical Flow Field

- linear springs are attached to the mechanical model, representing local optical flow computed via modified Lucas-Kanade method [5]
- the global optical flow is solved as a standard mechanics problem with a commercial FEM package
- resulting optical flow field reflects proper body mechanics for a chosen material law

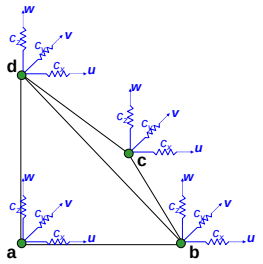

Local motion estimates (spring parameters):

$$\begin{bmatrix} N_{node}(x_i,y_i,z_i)\frac{\partial I(x_i,y_i,z_i)}{\partial x} & N_{node}(x_i,y_i,z_i)\frac{\partial I(x_i,y_i,z_i)}{\partial y} & N_{node}(x_i,y_i,z_i)\frac{\partial I(x_i,y_i,z_i)}{\partial z} \\ \vdots & \vdots & \vdots \\ N_{node}(x_n,y_n,z_n)\frac{\partial I(x_n,y_n,z_n)}{\partial x} & N_{node}(x_n,y_n,z_n)\frac{\partial I(x_n,y_n,z_n)}{\partial y} & N_{node}(x_n,y_n,z_n)\frac{\partial I(x_n,y_n,z_n)}{\partial z} \end{bmatrix}\begin{bmatrix} u \\ v \\ w \end{bmatrix}=\begin{bmatrix} N_{node}(x_i,y_i,z_i)\frac{\partial I(x_i,y_i,z_i)}{\partial t} \\ \vdots \\ N_{node}(x_n,y_n,z_n)\frac{\partial I(x_n,y_n,z_n)}{\partial t} \end{bmatrix}$$

Where $N_{node}(x,y,z)$ are linear element shape functions and (c_x,c_y,c_z) are confidence levels computed as:

$$c_x^{node}=\sum_{i=1}^{n}N_{node}(x_i,y_i,z_i)\left|\frac{\partial I(x_i,y_i,z_i)}{\partial x}\right|$$

FEM implementation

- 5-parameter poro-elastic constitutive law [2,3]
- Linear tetrahedral mesh
- Fluid flow modeled with temperature-displacement coupling
- Finite-deformation formulation
- Frictionless indenter-tissue boundary condition
- Modeled in ABAQUS 6.5-1 (HKS, Providence, RI)

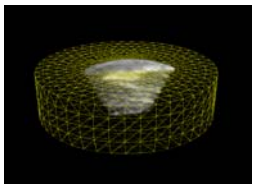

RESULTS & FUTURE WORK

Generation of Synthetic Data

- serves as "gold standard" for motion tracking validation
- 3D block of ultrasound texture from liver parenchyma
- texture block is deformed by uniaxial compression, assuming liver-like organ mechanics

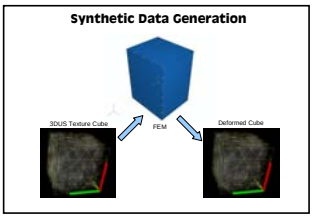

Motion Tracking Performance

- mechanical regularization provides superior accuracy to Horn & Schunck
- mechanical regularization has superior convergence characteristics
- both techniques perform well under noise (10% max-intensity white noise)

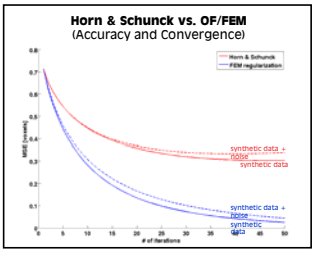

Future Work

- application of the motion tracking algorithm to soft tissue characterization
- investigation of parameter sensitivity under various imaging and testing conditions
- investigation of parameter uniqueness

ACKNOWLEDGMENTS

Funding by: U.S. Army Medical Research and Material Command, contract number DAMD 17-01-1-0677.

References:

[1] Kerdok AE, Jordan P, Liu Y, Wellman PS, Socrate S, Howe RD. Identification of Nonlinear Constitutive Law Parameters of Breast Tissue. Proc. of the 2005 Summer Bioengineering Conference, ASME, 2005.

[2] Socrate S, Boyce MC. A constitutive model for the large strain behavior of cartilage. In Proceedings of 2001 Bioengineering Conference, volume 50, pages 597-598. ASME, 2001.

[3] Febvay S, Socrate S. Biomechanical modeling of cervical tissue: a quantitative investigation of cervical funneling. In ASME Int. Mechanical Engineering Congress and Exposition (IMECE), 2003.

[4] Horn BPK, Schunck BG. Determining optical flow. Art. Intelligence, 16(1-3):186–203, August 1981.

[5] Lucas BD, Kanade T. An iterative image registration technique with an application to stereo vision. Proc. of the 7th Inter. Joint Conf. on Artificial Intelligence (IJCAI '81), pages 674–679, April 1981.